Cell Reports

Article

The E3 ubiquitin ligase FBXL6 controls the quality of newly synthesized mitochondrial ribosomal proteins

Graphical abstract

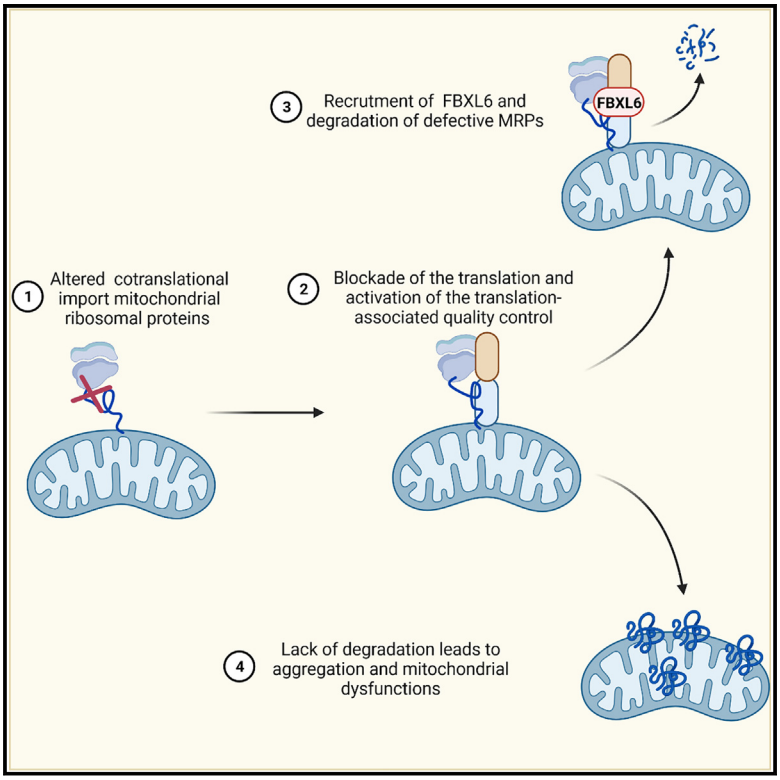

Highlights

- FBXL6 is a cytosolic E3 ubiquitin ligase contributing to mitochondrial functions
- FBXL6 ensures the quality of newly synthesized mitochondrial ribosomal proteins
- FBXL6 contributes to the translational-associated quality control

Authors

Julie Lavie, Claude Lalou, Walid Mahfouf, ..., Hamid Reza Rezvani, Richard Patryk Ngondo, Giovanni Bénard

Correspondence

giovanni.benard@inserm.fr

In brief

Lavie et al. find that FBXL6 contributes to mitochondrial health by controlling the quality of mitochondrial ribosome proteins prior to their import into the organelle. Moreover, they show that this mechanism is connected to the cytosolic translation-associated quality control and to the folding of newly synthesized proteins.

Lavie et al., 2023, Cell Reports *42*, 112579
June 27, 2023
https://doi.org/10.1016/j.celrep.2023.112579

CellPress

Cell Reports

CellPress
OPEN ACCESS

Article

The E3 ubiquitin ligase FBXL6 controls the quality of newly synthesized mitochondrial ribosomal proteins

Julie Lavie,[1,2] Claude Lalou,[1,2] Walid Mahfouf,[2,3] Jean-William Dupuy,[2,4] Aurélie Lacaule,[1,2] Agata Ars Cywinska,[1,2] Didier Lacombe,[1,2,5] Anne-Marie Duchêne,[6] Anne-Aurélie Raymond,[2,3,7] Hamid Reza Rezvani,[2,3] Richard Patryk Ngondo,[6,8] and Giovanni Bénard[1,2,9,*]

[1]Laboratoire Maladies Rares: Génétique et Métabolisme, INSERM U1211, 33076 Bordeaux, France
[2]Université de Bordeaux, 33000 Bordeaux, France
[3]Université de Bordeaux, INSERM, UMR1312, Bordeaux Institute of Oncology, Bordeaux, France
[4]Université de Bordeaux, Plateforme Protéome, 33000 Bordeaux, France
[5]CHU Bordeaux, Service de Génétique Médicale, 33076 Bordeaux, France
[6]Université de Strasbourg, CNRS, Institut de Biologie Moléculaire des Plantes, UPR2357, 67000 Strasbourg, France
[7]Plateforme Oncoprot, TBM-Core US 005, 33000 Bordeaux, France
[8]Université de Strasbourg, CNRS, Architecture et Réactivité de l'ARN, UPR9002, 67000 Strasbourg, France
[9]Lead contact
*Correspondence: giovanni.benard@inserm.fr
https://doi.org/10.1016/j.celrep.2023.112579

SUMMARY

In mammals, about 99% of mitochondrial proteins are synthesized in the cytosol as precursors that are subsequently imported into the organelle. The mitochondrial health and functions rely on an accurate quality control of these imported proteins. Here, we show that the E3 ubiquitin ligase F box/leucine-rich-repeat protein 6 (FBXL6) regulates the quality of cytosolically translated mitochondrial proteins. Indeed, we found that FBXL6 substrates are newly synthesized mitochondrial ribosomal proteins. This E3 binds to chaperones involved in the folding and trafficking of newly synthesized peptide and to ribosomal-associated quality control proteins. Deletion of these interacting partners is sufficient to hamper interactions between FBXL6 and its substrate. Furthermore, we show that cells lacking FBXL6 fail to degrade specifically mistranslated mitochondrial ribosomal proteins. Finally, showing the role of FBXL6-dependent mechanism, FBXL6-knockout (KO) cells display mitochondrial ribosomal protein aggregations, altered mitochondrial metabolism, and inhibited cell cycle in oxidative conditions.

INTRODUCTION

The mitochondria proteome contains about 1,000–1,500 proteins.[1] In mammals, only 13 of these mitochondrial proteins are directly encoded and translated inside the organelle, and they contribute exclusively to the oxidative phosphorylation (OXPHOS) complexes. Thus, the large majority of mitochondrial proteins are encoded by nuclear genes, translated in the cytosol and imported to the various compartments of this organelle, and contribute to the different mitochondrial functions. Translation and import of these nuclear gene-encoded mitochondrial proteins is facilitated by the proximity between the cytosolic ribosomes and the outer mitochondrial membrane (OMM),[2,3] and it was proposed that the cytosolic ribosomes are physically connected to the translocase of the outer mitochondrial membrane (TOM) through specific receptors.[4] The cytosolic translation and import through the outer membrane represent two important sites regarding protein quality control.

Indeed, at the level of the organelle, the TOM complex coordinates the autophagic degradation of defective mitochondria by mitophagy through the stabilization of the serine/threonine-protein kinase PINK1 at the outer membrane.[5] TOM is also the receptor of molecular chaperones such as heat shock protein (HSP) 90 and HSP70 that are known to promote the ubiquitin-dependent clearance of defective newly synthesized proteins.[6,7] Notably, this mechanism prevents incorporation of defective proteins. In this line, Mohanraj et al.[8] showed that the mutated mitochondrial protein COA7 has a slower mitochondrial import rate and that mislocalized proteins are degraded in the cytosol by the proteasome. Therefore, blockade of mitochondrial protein import triggers proteostasis stress, including activation of the unfolded protein response and upregulation of HSPs.[9,10] Regarding the cytosolic side, ribosomes represent a major platform that orchestrates mRNA and nascent chain quality control.[11] As shown by Duttler et al.,[12] the quality of nascent and newly synthesized proteins is ensured by a clever balance between folding and ubiquitin-dependent degradation, and this mechanism is rendered possible by the mobilization of a complex network of E3 ubiquitin ligases and chaperones physically associated with the ribosome. Accordingly, defective translation

and ribosome stalling trigger a specific mechanism called ribosome-associated quality control (RQC), which involves a complex and conserved machinery.[13] In this process, the E3 ubiquitin ligase listerin (Ltn1/LTN1) is recruited to the 60S ribosomal subunit in order to ubiquitinate aberrant proteins resulting from defective translation.[14] Recently, Izawa et al. unified the cytosolic ribosome- and the OMM-associated quality control through a mechanism that they named mitochondrial ribosome-associated protein quality control (mitoRQC).[15] Using a yeast model, they demonstrated that the VCP/CDC48-associated mitochondrial stress-responsive protein 1 (Vms1) acts together with the E3 ubiquitin ligase Ltn1 and the ribosome quality control complex subunit 2 Rqc2 to protect mitochondria from toxic aggregations of defective nascent proteins. This mitoRQC is essential for mitochondrial metabolic functions in yeast since the deletion of Vms1 hampers the cell growth under oxidative conditions.[15,16]

Notably, in mammalian cells, the existence of the mitoRQC has not yet been described, but this mechanism is highly credible. Indeed, most of proteins involved in the RQC are conserved from yeast to higher eukaryotes. Interestingly, it was shown that mitochondrial damage blocks the translation of mitochondrial proteins and leads to the recruitment of protein pelota homolog (PELO) and ATP-binding cassette sub-family E member 1 (ABCE1),[17] and these proteins are known to have a crucial role in the RQC.[18] In the same way, the mammalian homolog of Vms1, ANKZF1 (Ankyrin repeat and zinc-finger domain-containing protein 1), was reported to translocate to the mitochondria under oxidative stress.[19] In our study, we investigated the function of the E3 ubiquitin ligase, F box/leucine-rich repeat protein 6 (FBXL6) using mammalian cells. We propose that FBXL6 participates in the quality control of mitochondrial ribosomal proteins in coordination with the cytosolic ribosome quality-control hub. We found that that this enzyme interacts physically with *de novo*-synthesized ribosomal proteins, including mitochondrial proteins. On the other hand, FBXL6 also binds RQC proteins and chaperones involved in the folding and transport of newly synthesized proteins. Showing the importance of this mechanism, deletion of FBXL6 leads to defective mitochondrial metabolism.

RESULTS

FBXL6 is implicated in mitochondrial biogenesis during the cell cycle

FBXL4 is an E3 ubiquitin ligase, mutations of which are responsible for the mitochondrial DNA depletion syndrome 13, and this syndrome is characterized by inhibited mitochondrial energy metabolism.[20–22] Our results showed that the CRISPR-Cas9-mediated deletion of this enzyme in HeLa cells (FBXL4-knockout [KO]) specifically impaired the mitochondrial metabolism leading to inhibition of the cell growth in oxidative conditions but not in glycolytic conditions (Figures 1A, 1B, S1A, and S1B).[23,24] Interestingly, we found that cells carrying deletion of FBXL6, another member of the FBXL family, displayed the same cell growth discrepancy, suggesting a mitochondrial metabolic dysfunction (Figures 1A, 1B, S1C, and S1D). Effects on cell growth were rescued by FBXL6 ectopic expression in KO cells (Figure S1E). Furthermore, we found that FBXL4- and FBXL6-KO cells were blocked in the G2/M phase of the cell cycle under oxidative conditions but not when cultured in medium containing glucose (Figures 1C and 1D). To confirm that these growth defects resulted from impaired mitochondrial metabolic functions, we measured the oxygen consumption rates (OCRs) and mitochondrial ATP production in FBXL6-KO cells (Figures 1E and 1F). These cells displayed moderate decreases of endogenous OCR and these values were comparable with inhibition measured for FBXL4-KO cells (Figures 1E and S1F). On the other hand, mitochondrial ATP production was inhibited by about 30% in FBXL6-KO cells and by 25%–40% in FBXL4-KO cells, supporting impaired coupling efficiency between oxygen consumption and ATP production (Figure 1F). To understand the causes of these mitochondrial alterations, we analyzed the remodeling of biological pathways in FBXL6-KO by whole-cell proteomics (Figure 1G; Table S1), and our results revealed upregulation of proteins involved in ribosome biogenesis (Figure 1H; Table S1). Concomitantly, using immunoblots, we found that FBXL6 deletion was associated with decreased levels of cytochrome *c* oxidase subunit 2 (MT-CO2) and, notably, higher levels of some mitochondrial proteins, such as NDUFS3 or the mitochondrial ribosomal protein L45 (MRPL45) (Figures S1G and H). These results show that FBXL6, like FBXL4, participates in the mitochondrial functions through the regulation of mitochondrial protein contents.

FBXL6 is not an intrinsic mitochondrial E3 ubiquitin ligase

In silico predictions for mitochondrial localization computed by iPSORT, mitoprot, or targetP revealed that FBXL6 had a better theoretical mitochondrial score than FBXL4 (Table S2). However, no experimental evidence for a mitochondrial localization was reported in mitoCarta databases (Table S1). By immunofluorescence, we found that FBXL6 displayed a diffused localization in the cytosol and in the nucleus (Figures 2A and 2B; Pearson's coefficient Myc vs. TOMM20 = -0.01 ± 0.02). The nuclear localization represented 46.8% ± 3.5% of the cell population and 53.21% ± 3.6% for the cytosolic distribution ($n = 5$, $p = 0.24$, unpaired t test). In comparison, FBXL4 localized to the mitochondria (Pearson's coefficient Myc vs. TOMM20 = 0.90 ± 0.01). FBXL3, another E3 ubiquitin ligase from the same family displayed a strictly nuclear localization (Figures 2A and 2B), as previously reported.[25] To further confirm that this E3 is not an intrinsic mitochondrial protein, we assayed the presence of a leading sequence by coupling the N-terminal amino acids of FBXL4 (1–25 amino acids) and FBXL6 (1–20 amino acids) to green fluorescent protein (GFP). The N-terminal sequence of FBXL4 was sufficient to target the GFP to the mitochondria, while the FBLX6 one failed to address the fluorescent reporter to any specific subcellular compartment (Figures 2C and 2D). These results support that FBXL6 does not contain a mitochondrial leading sequence (MLS). Then, using cell fractionation assays, we confirmed that FBXL6 had a spread subcellular localization (Figure 2E). Nevertheless, a part of FBXL6 was retained to the mitochondrial purified fraction, free of associated membranes (Figure 2E). This part of FBXL6 was quickly digested during a trypsin accessibility assay, suggesting that it was loosely associated with the organelle surface, facing the cytosol (Figure 2F). Taken together, these results support that FBXL6 is not an

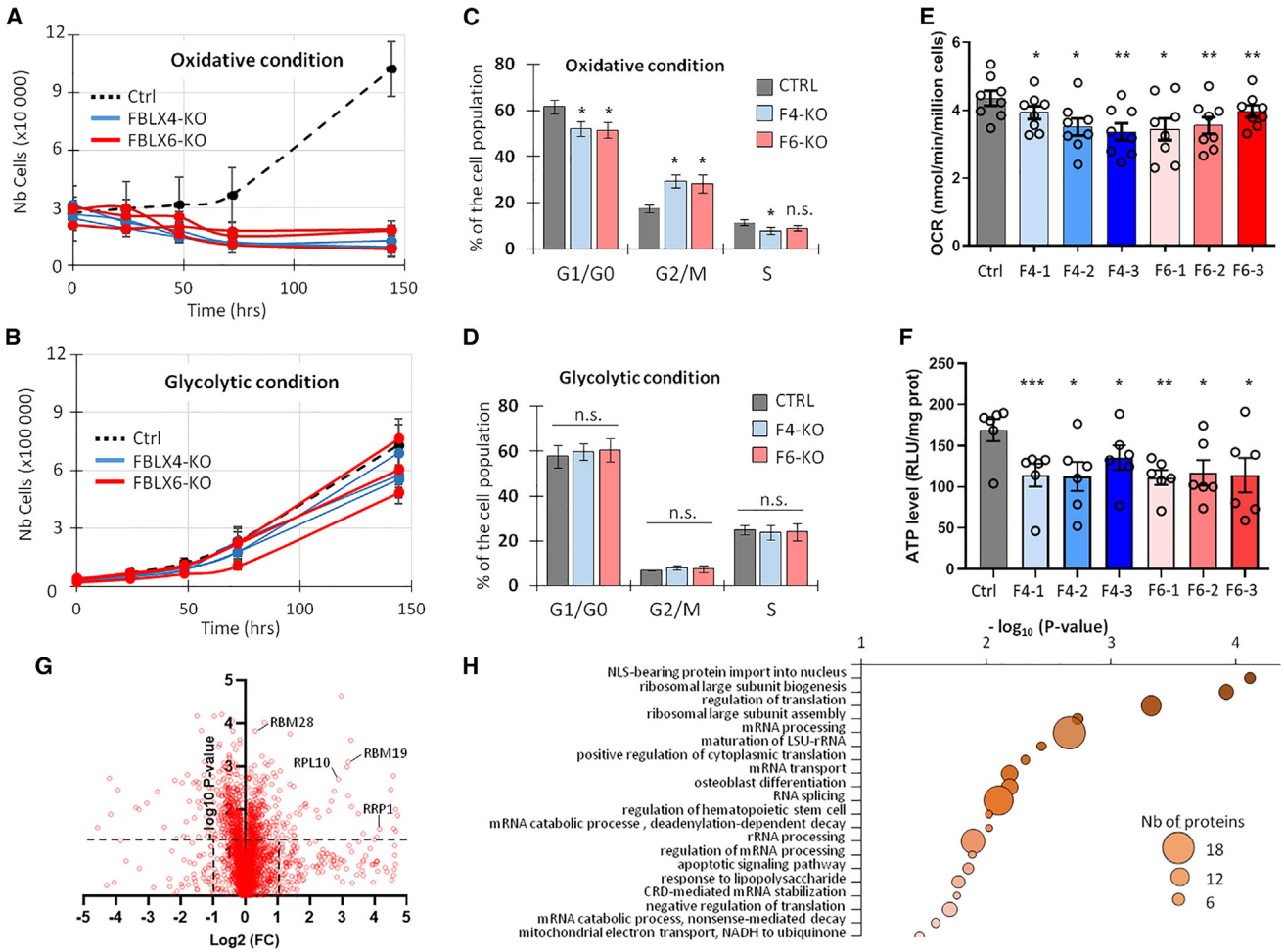

Figure 1. KO of FBXL4 and FBXL6 causes mitochondrial defects and cell cycle perturbations

(A and B) Growth of FBXL6-KO (red), FBXL4-KO (blue), and control (dashed black) cells were measured under glycolytic (A) and oxidative (B) conditions. Growth was measured in three different FBXL4- or FBXL6-KO HeLa cell clones (means ± SEM, n = 3 for each clone).

(C and D) Cell-cycle analyses performed on FBXL4-KO, FBXL6-KO, and control cells grown under oxidative (C) or glycolytic (D) conditions (means ± SEM, n = 4–8, *p < 0.05, ANOVA Kruskal-Wallis test).

(E and F) Basal oxygen consumption rates (OCRs) (E) and mitochondrial ATP levels (F) of FBXL4-KO (blue shade), FBXL6-KO (red shade), and control (black) cells. Bars indicate the means ± SEM for the different KO clones, and open circles represent single measurements. *p < 0.05, **p < 0.01, repeated measures (RMs) ANOVA-Holm-Sidak's multiple comparisons test. For OCR, n = 8 and for ATP level, n = 6.

(G) Proteomic analyses of FBXL6-KO and control whole-cell extracts cells by using mass spectrometry. Graphs represent the volcano plots obtained by comparing the differential protein expression between FBXL6-KO and control cells. Each symbol represents an identified protein (n = 3). Examples of proteins involved in the mitochondrial functions or in the ribosome biogenesis are cited.

(H) Gene Ontology enrichment analyses of upregulated proteins in FBXL6-KO vs. control cells. Pathways are represented according to −log10 of p value (abscissa axis). The circle size is proportional to the number of proteins.

inherent mitochondrial protein, but it can be loosely linked to the organelle surface.

FBXL6 regulates newly synthesized ribosomal proteins

To study the FBXL6-dependent mechanism, we analyzed the interactome of the E3 by co-immunoprecipitations coupled to mass spectrometry. We found that FBXL6 interacted with 451 proteins (Figure 3A; Table S3). Considering annotated biological functions, Gene Ontology analyses revealed that the cytosolic/mitochondrial translation was the most represented pathway among the FBXL6 partners (42 proteins; Figure 3B; Table S4). Indeed, FBXL6 interacted with both cytosolic and mitochondrial ribosomal proteins (e.g., RPL7, RPL17, MRPL37, or MRPL28) and these proteins represented the most abundant type of proteins that interact with this E3. As expected, FBXL6 also interacted with proteins implicated in the ubiquitin proteasome pathway (23 proteins) and, specifically, SKP1, RBX1, and CULLIN-1, confirming that this E3 can form the SCF complex (SKP1-CULLIN1-FBXL6) like other FBXLs. Then, FBXL6 also significantly bound proteins involved in the protein folding pathway (32 proteins). These proteins included numerous chaperones and co-chaperones required for the folding

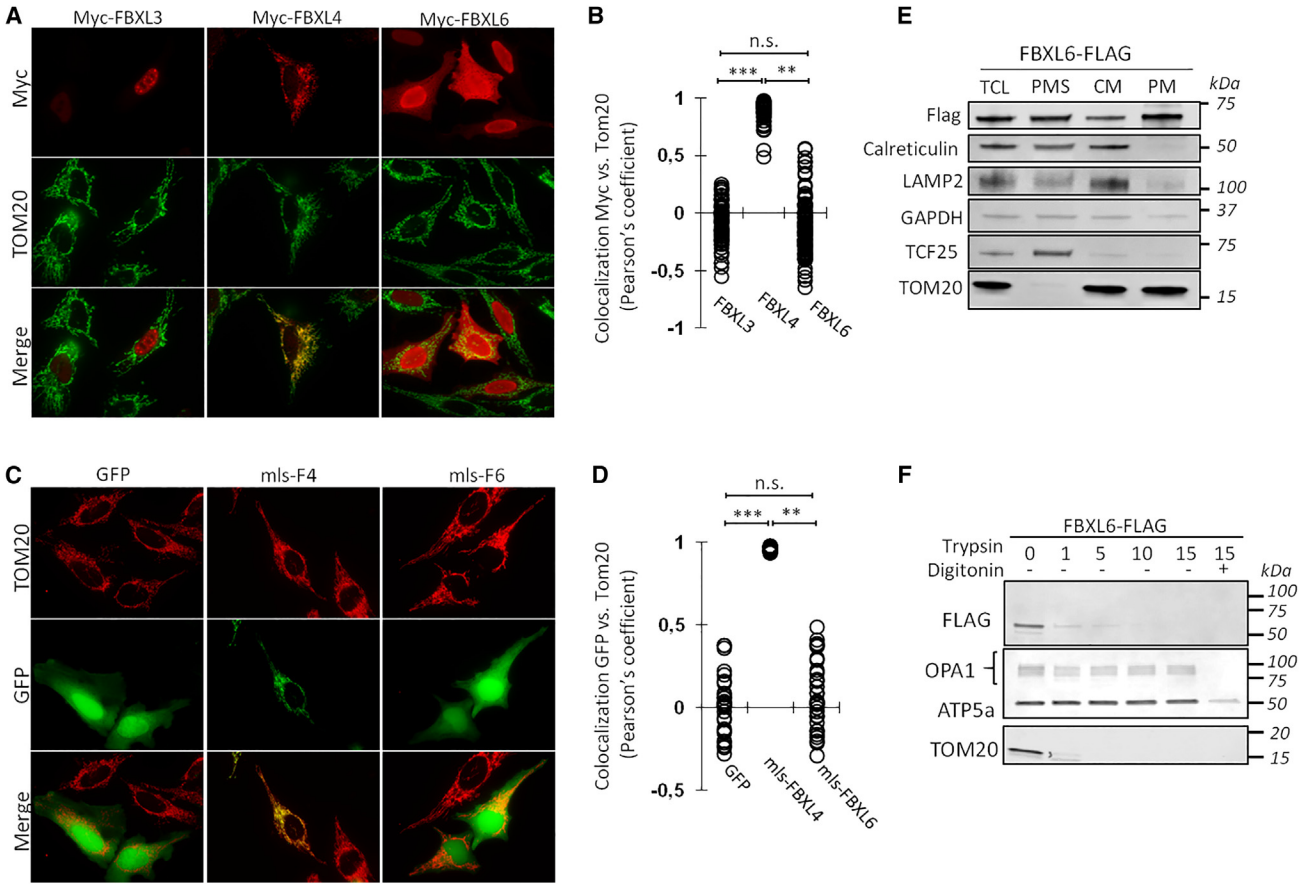

Figure 2. FBXL6 is located in the cytosol and the nucleus

(A) Immunofluorescence performed on HeLa cells ectopically expressing Myc-tagged FBXL3, FBXL4, or FBXL6. FBXL mitochondria were labeled using anti-Myc (red) and anti-translocase of the outer mitochondrial membrane 20 (TOMM20) (green) antibodies, respectively.

(B) Quantification of FBXL localization to mitochondria obtained from (A). Pearson's correlation coefficient between the TOMM20 and Myc staining; each dot represents the value for one cell (n = 4–6, 70–100 cells, ***$p < 0.001$ ANOVA, Kruskal-Wallis test).

(C) Immunofluorescence performed on HeLa cells expressing green fluorescent protein (GFP) fused to the theoretical mitochondrial leading sequence of FBXL4 or FBXL6. Mitochondria were labeled using an anti-TOMM20 antibody.

(D) Quantification of the chimeric GFP targeted to the mitochondria from (C). Each dot represents the Pearson's correlation coefficient for single cells (n = 3, 40–60 cells, ***$p < 0.001$ ANOVA, Kruskal-Wallis test).

(E) Immunoblots performed using the total cell lysate (TCL), post mitochondrial supernatant (PMS), crude mitochondria (CM), and purified mitochondria (PM). Fractions were obtained from HEK cells expressing FBXL6-FLAG. FBXL6 was detected using anti-FLAG. Calreticulin, LAMP2, GAPDH, TCF25, and TOM20 were used as marker of the endoplasmic reticulum (ER), lysosomes, cytosol, nucleus, and mitochondria, respectively.

(F) Immunoblots showing the results of the trypsin accessibility assay performed on mitochondria isolated from HEK cells expressing FBXL6-FLAG. OPA1 mitochondrial dynamin such as GTPase (OPA1), ATP5A, and TOMM20 were used as respective markers of the intermembrane space and the inner and the outer mitochondrial membranes.

and transport of newly synthetized proteins (e.g., HSPA8, HSPA1A/B, HSP90AB1, BAG2) and implicated in delivering of newly synthesized protein to mitochondria (HSP90AA1).[6] Finally, we found interactions with the RQC proteins NEMF and PELO (Figure 3A).[18,26]

These results were validated by using other approaches. First, by immunoblots coupled to immunoprecipitation (IP), we showed that FBXL6 and also FBXL4 interacted with SKP1 or HSPA1A. We also confirmed that FBXL6 binds mitochondrial ribosomal proteins such MRPL45 and MRPL42, and this was not the case for other members of the FBXL family such as FBXL4 or FBXL3 (Figure 3C and S2A). Second, because E3 ubiquitin ligases have labile and transient interactions with their substrates and partners, we analyzed the FBXL6 interactome using a biotin proximity labeling assay based on TurboID.[27] HCT116 cells expressing stably GFP-TurboID or FBXL6-TurboID (Figures S2B and S2C) were treated with biotin for 0.5 or 16 h (Figures S2D–S2F). Biotinylated proteins were identified by mass spectrometry after streptavidin pull-down (Figures S2E and S2F). After 16 h, 120 interacting proteins were identified and, compared with FLAG pull-down, this lower number of interacting proteins suggests a steric hindrance due to the presence of the TurboID. Nevertheless, these proximity labeling assays confirmed that FBXL6 interacts with mitochondrial proteins,

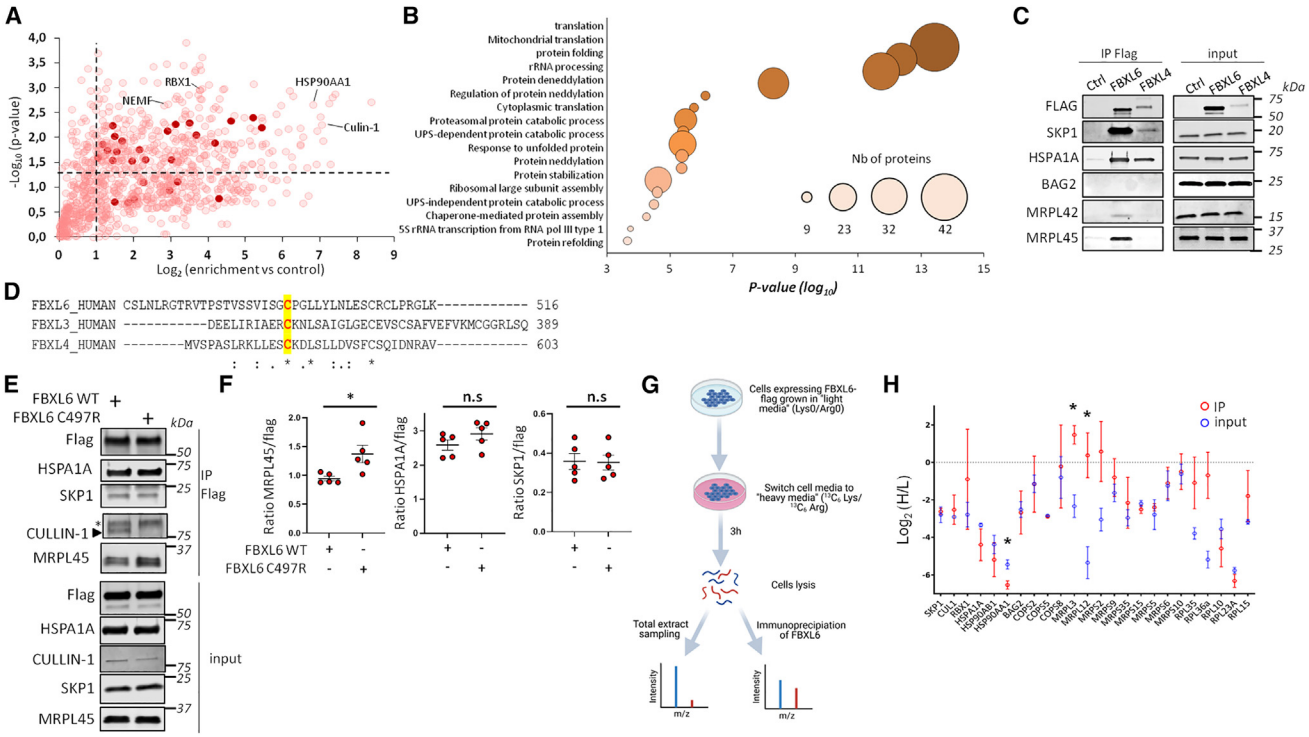

Figure 3. Identification of FBXL6-interacting proteins

(A) HEK cells were transfected with β-gal (control) or FBXL6-FLAG. After FLAG immunoprecipitation (IP), interacting proteins were identified using mass spectrometry. Plots representing the fold changes (log_2) and p values ($-log_{10}$) for proteins interacting with FBXL6 vs. control. The names of proteins of interest are specified. Dark red red dots are mitochondrial ribosomal proteins. n = 3 independent IPs.

(B) Gene Ontology enrichment analyses performed on FBXL6-interacting proteins. Enriched pathways are displayed with log_{10} of p value (abscissa axis). The circle size is proportional to the number of counted proteins.

(C) HEK cells transfected with β-gal (control), FBXL4-FLAG, and FBXL6-FLAG and IP performed using an anti-FLAG antibody. Immunoprecipitated proteins were analyzed using immunoblots (n = 6). Interactions with proteins were analyzed by immunoblots (see details in the panel).

(D) FBXL3, 4, and 6 amino acid sequences of alignment. Substrate-binding domains are represented and a conserved cysteine highlighted.

(E and F) IP of WT- or C497R-FBXL6 FLAG. WT- or C497R-FBXL6 FLAG were expressed in HEK cells and interactions with various SKP1, HSPA1A, and MRPL45 were analyzed by immunoblots (E). Graphs represent quantification immunoblots, and values are normalized to the FLAG level (F). (n = 5, *p < 0.05, unpaired t test).

(G) Pulsed SILAC experimental design. HeLa cells expressing FBXL6 grown in light (L, R0K0) medium were transferred to heavy (H, R10K8) medium for 3 h. Samples of the total fractions (input) were collected and IPs of FBXL6 (IP) performed in parallel. The H/L ratios were determined by mass spectrometry.

(H) H/L ratio determined for FBXL6-interacting proteins in input (blue) or after IP (red). Ratios were expressed as log2. Blue and red bars correspond to H/L ratio measured in input or IP fractions, respectively (n = 3, *p < 0.05, unpaired t test).

including mitochondrial ribosomal proteins (e.g., MRPS35, MRPS9) (Figure S2G; Table S5).

Next, we detailed FBXL6-interacting properties by targeting its substrate-binding domain. Indeed, FBXL6, 3, and 4 contain a conserved cysteine in the substrate-binding domain (Figure 3D),[28] and mutations of this cysteine to an arginine in FBXL4 (C584R) and FBXL3 (C358R) are responsible for specific rare diseases.[29,30] The mutation of this conserved amino acid in FBXL6 (C497R) did not affect the ability of FBXL6 to bind HSPA1 or SKP1 (Figures 3E and 3F). However, it increased interaction with the MRPL45, indicating that the release of this substrate protein was blocked (Figures 3E and 3F). This blockade induced the release of SKP1-FBXL6 from the SCF since mutated FBXL6 did not associate with CULLIN-1 (Figures 3E and 3F).

Since FBXL6 is not a mitochondrial E3 (see Figure 2), we postulated that FBXL6 interactions with mitochondrial ribosomal proteins occurred in the cytosol with *de novo*-synthesized proteins. To assess this hypothesis, we analyzed whether FBXL6 had preferential interactions with newly synthesized proteins using a stable isotope labeling by amino acids in cell culture (SILAC) approach. Cells expressing FBXL6 were incubated for 3 h with heavy SILAC medium, and we measured enrichment of labeled proteins in both input and FBXL6 immunoprecipitated fractions (Figure 3G). After SILAC treatment, proteins have incorporated about 10% of heavy amino acids, and this level was not affected either by IP procedures or by the FBXL6 expression (Figure S2H). We measured the difference in SILAC labeling between inputs and pulled-down fractions when we compared SILAC labeling levels of FBXL6 constitutive partners such as SKP1, CULLIN-1, or HSPs proteins (Figure 3H). However, various cytosolic or mitochondrial ribosomal proteins such as RPL35, RPL36a, MRPL3, and MRPL12 displayed enriched SILAC labeling in IP fractions compared with inputs indicating

that FBXL6 interacted preferentially with newly synthesized ribosomal proteins (Figure 3H).

FBXL6 is involved in the degradation of defective proteins

Identification of FBXL6 partners as well as its preferential binding to newly synthesized proteins suggest that this E3 participates in protein quality control associated with the translation. To test this hypothesis, we generated a GFP carrying an $(Ala\text{-}Thr)_{10}$ extension at the C terminus to mimic C-terminal alanine and threonine (CAT)-tailed proteins, which are obtained upon activation of the RQC.[31,32] These chimeric proteins were targeted either to the mitochondria (mtGFP-CAT) or to the cytosol (cGFP-CAT). Like a previous report by Izawa et al. in a yeast model,[15] cGFP-CAT formed SDS-resistant aggregates and, notably, this was also the case with mt-GFP-CAT (Figure S3A). Inhibition of the proteasome promoted these aggregates (Figure S4A). Regarding the cellular localization, cGFP-CAT aggregated in precise foci within the cytosol, whereas the control cGFP displayed a homogeneous cytosolic distribution (Figure S3B). We observed that mtGFP-CAT also formed aggregates and that these aggregates were located in the mitochondria (Figure S3C). Epoxomicin-induced proteasome inhibition dramatically increased the formation of aggregates in the cytosol but also in the mitochondria. Accordingly, these results showed that the RQC and the ubiquitin-dependent degradation also prevent accumulation of defective newly synthesized mitochondrial proteins in mammalian cells.

Because GFPs are xenoproteins that are particularly stable in mammalian cells that tend to naturally aggregate, we developed a similar approach using the FBXL6 endogenous substrate MRPL45. We generated a CAT-tailed and a stop codon deleted MRPL45 (MRPL45-CAT or -NS, respectively). First of all, these defective MRPL45s were highly unstable compared with wild-type (WT) MRPL45 or with GFP-based constructs (Figure 4A). Notably, MRPL45-CAT or -NS can be imported to the mitochondria, but, under inhibition of the proteasome by epoxomicin, colocalization of these defective proteins with the organelle was decreased (Figures S3D and S3E). This result supported that a portion of these proteins are eliminated in a proteasome-dependent manner during their import and inhibition of the proteasome induced their cytosolic accumulation. Then, since E3s are highly dynamic enzymes that change localizations following the activation state, we analyzed whether expression of these proteins affects the FBXL6 localization. FBXL6 displayed a spread cytosolic distribution in cells expressing WT-MRPL45, and no colocalization with the mitochondrial ribosomal protein was observed (Figures 4B and 4C). Notably, expression of MRPL45-CAT and MRPL45-NS induced translocation of FBXL6 to precise cytosolic foci, and the degree of colocalization between the E3 and defective proteins significantly improved (Figures 4B and 4C). These results suggest that the FBXL6-dependent mechanism is triggered by the presence of altered ribosomal proteins mimicking a defective translation.

Next, we tested whether FBXL6 is involved in the degradation of these defective proteins. FBXL6-KO and control cells were transfected with either WT or CAT-tailed MRPL45 and treated with cycloheximide to block the protein synthesis and epoxomicin to inhibit proteasome-dependent degradation. Degradation rate of WT-MRPL45 was not significantly affected by deletion of FBXL6 (Figure 4D). MRPL45-CAT was promptly eliminated in control cells, but it was hampered in FBXL6-KO cells (Figure 4E). Addition of epoxomicin inhibited these degradations. Hence, the half-life of MRPL45-CAT increased by 3-fold in FBXL6-KO compared with control cells (Figures 4F and 4G). Interestingly, this inhibition was also measured in FBXL4-KO cells, supporting that this E3 is also involved the control quality of mitochondrial proteins (Figures 4D–4G). Similar data were obtained when we compared the degradation rate of CAT-tailed vs. WT MRPL42 in control and FBXL6-KO cells (Figures S4A and S4B). To specifically test FBXL6 regarding defective mitochondrial ribosomal proteins, we performed same experiment using a CAT-tailed version of the subunit A of the mitochondrial succinate dehydrogenase (SDHA-CAT), and no difference in degradation was found between control, FBXL4-KO, and FBXL6-KO cells (Figure S4C). Regarding MRPL45-NS, the defective protein was very rapidly degraded and displayed a very short half-life, making it difficult to assess the effect of the deletion of FBXL6 (Figure S4D). However, we found that the deletion of FBXL6 potentiated MRPL45-NS accumulation induced by the proteasome inhibition, and this result supports that FBXL6 also participated in the proteasome-dependent degradation of the non-stop protein (Figures 4H and 4I).

Finally, we measured effects of MRPL45-CAT expression on mitochondrial respiration in control and FBXL6-KO cells. In control cells, we found that expression of MRPL45-CAT did not significantly affect the OCR compared with WT MRPL45 (Figure 4J). FBXL6-KO cells expressing WT MRPL45 displayed decreased OCR compared with control cells, which confirms that these cells had lower mitochondrial activities in basal condition as we reported above. More interestingly, expression of MRPL45-CAT further inhibited the mitochondrial respiration by 33%, showing that the accumulation of defective proteins can alter mitochondrial function in the absence of an FBXL6-dependent mechanism. These results reveal the importance of the FBXL6-dependent mechanism regarding mitochondrial health.

Implications of RQC proteins and chaperones in the FBXL6-dependent mechanism

Beside ribosomal proteins, we have identified that FBXL6 interacts with different partners, including HSPs and RQC proteins. Accordingly, we analyzed the contribution of these partners to the FBXL6-dependent mechanism. First, we focused on proteins of the RQC.

FBXL6 interacted with proteins involved in the initial steps of the RQC, including ZNF598, PELO, and to a lesser extent NEMF, but no interaction was reported with proteins associated with the degradation of defective nascent proteins such as TCF25, VCP, or LTN1 (Figure 5A). Hence, FBXL6 interacted with proteins involved in the sensing of the ribosome stalling.[13] First, we analyzed whether these proteins can affect the ability of FBXL6 to bind MRPL45 by IP assays. We focused on LTN1, which ubiquitinates defective proteins, and NEMF, which is required to sense the ribosome stalling and to add the CAT tail. Lack of NEMF also specifically inhibited interactions between FBXL6 and its substrate, MRPL45, or its partner,

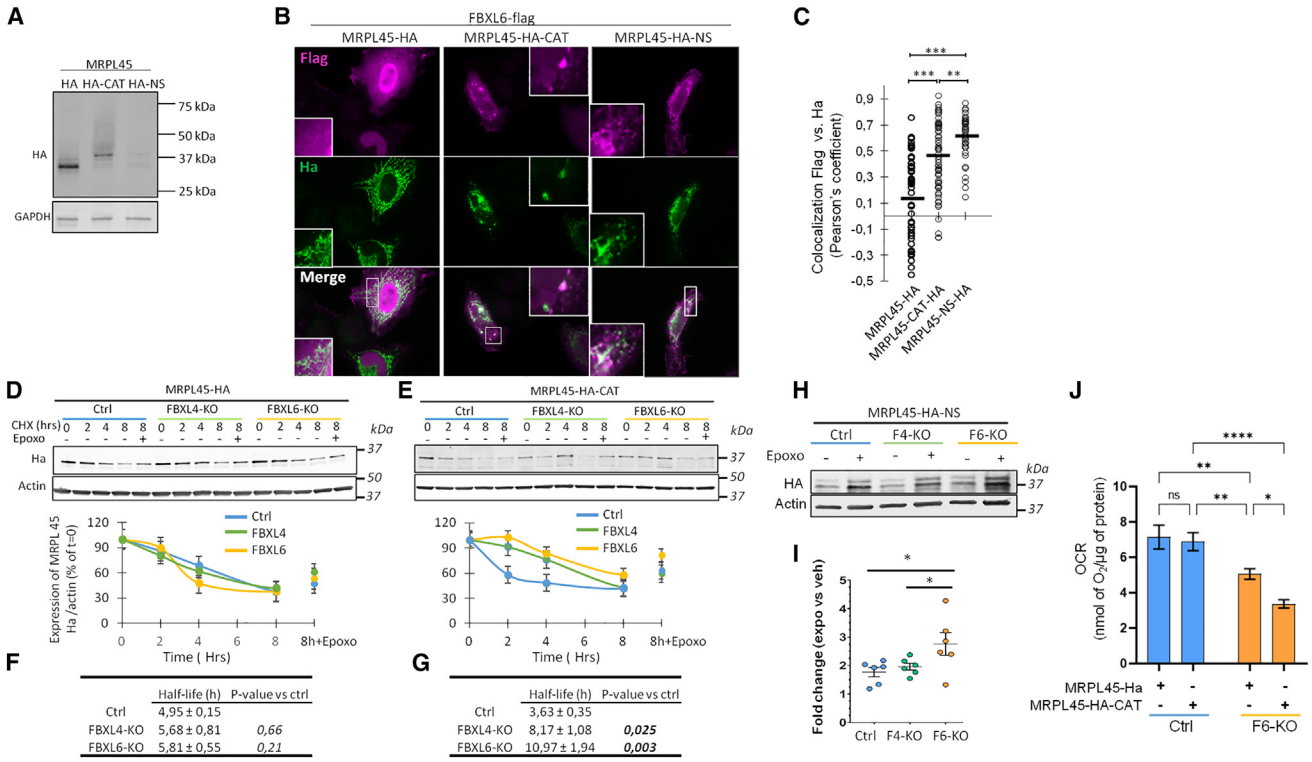

Figure 4. FBXL6 is involved in the degradation of defective MRPL45

(A) Immunoblot showing expression of MRPL45-hemagglutinin (HA), MRPL45-HA-CAT, and MRPL45-HA-NS in HEK cells using anti-HA antibody.

(B) Immunofluorescence performed on HeLa cells expressing FBXL6-FLAG and transfected with mitochondrial ribosomal protein L45 (MRPL45)-HA, MRPL45-HA-CAT, or MRPL45-HA-lacking a stop codon (NS). MRPL45 and FBXL6 were labeled using anti-HA and anti-FLAG antibodies, respectively.

(C) MRPL45 and FBXL6 colocalization was quantified by measuring the Pearson's correlation coefficient between HA and FLAG labeling. Each dot is the value for one cell (n = 3–4, 60–120 cells, ***p < 0.001, **p < 0.01, ordinary one-way ANOVA, Holm-Sidak test).

(D and E) FBXL6-KO, FBXL4-KO, and control cells were transfected with MRPL45-HA (D) or MRPL45-HA-CAT (E) and treated with cycloheximide for 0, 2, 4, and 8 h. The protein levels of MRPL45-HA and MRPL45-HA-CAT were evaluated using immunoblots. The plots show protein quantification normalized to that of t = 0 (n = 4).

(F and G) The calculated half-life of each protein is summarized in the table under the graph. First-order approximation was used for this calculation. (n = 4, RM ANOVA, Fisher test).

(H and I) Accumulation of MRPL45-HA-NS was analyzed in FBXL6 KO, FBXL4-KO, and control cells. Cells expressing MRPL45-HA-NS were treated with epoxomicin for 8 h. Levels of MRPL45-HA-NS were revealed by immunoblots using anti-Ha (H). MRPL45-HA-NS levels were normalized to actin and expressed as fold change of untreated control cells (I) (n = 6, *p < 0.05, two-way ANOVA).

(J) Basal OCRs measured in control (blue bars) and FBXL6-KO (yellow bars) cells transfected with WT MRPL45-HA and MRPL45-HA-CAT. Values are normalized to the micrograms of proteins (n = 20, *p < 0.05, ***p < 0.001, **p < 0.01, two-way ANOVA).

HSPA1A. These interactions were not fully abolished (Figures 5B and 5C). Of note, FBXL6 ectopic expression is reduced in NEMF-KO cells. In LTN1-KO cells, interactions with MRPL45 or HSPA1A were not affected, but we observed a stabilization of the SCF complex characterized by a higher association of FBXL6 with SKP1 (Figures 5B and 5C). Using LTN1/NEMF double KO, we showed that this effect requires NEMF. Data obtained through transient silencing showed that other RQC proteins are affected by FBXL6 interactions with MRPL45 (Figure S5A). Second, we analyzed the FBXL6 localization upon deletion of NEMF, LTN1, and NEMF/LTN1. Interestingly, deletion of these proteins modified FBXL6 subcellular localization by inducing its relocation to cytosolic cluster as we observed upon expression of MRPL4545-CAT and MRPL45-NS (Figures 5D and 5E, see also Figure 4B). We did not observe this phenotype when we expressed GFP in these KO cells (Figures 5E and S5B). Thus, the translational stress generated by lack of RQC response triggered the FBXL6-dependent mechanism. Finally, we assessed whether FBXL6 and RQC proteins could act synergistically. Upon silencing of LTN1, MRPL45 tended to accumulate in FBXL6-KO (18.2% ± 0.06%), but this difference was not significant (n = 4, p value FBLX6-KO vs. control = 0.0706). In contrast, downregulation of NEMF decreased the level of endogenous MRPL45 by 23.5% ± 0.04% in FBXL6-KO compared with control cells (n = 4, p value FBLX6-KO vs. control = 0.0105), suggesting a coordinated action of NEMF and FBXL6 (Figures S5C and S5D). In addition, we found that MRPL45-NS accumulates in control cells treated with epoxomicin for 0, 4, and 8 h. (Figure 5F) and this buildup included formation of a lower-molecular form of MRPL45-NS as previously reported.[31] Accumulation of

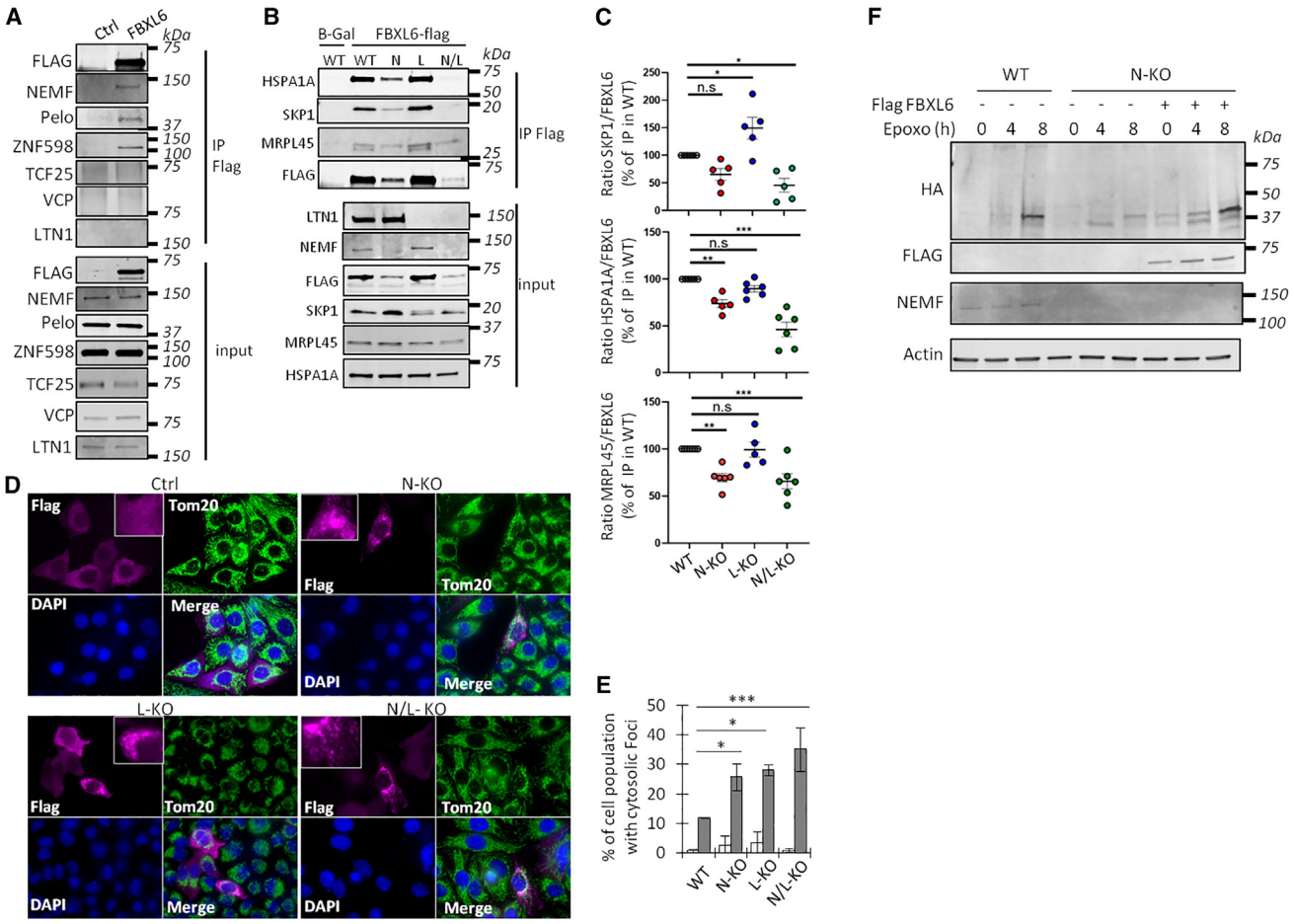

Figure 5. FBXL6 is involved in the RQC pathway

(A) Interactions of FBXL6 with RQC proteins were analyzed by FLAG IP using cells transfected with FBXL6 FLAG or control (β-gal). Interaction with NEMF, PELO, and ZNF598 were revealed by immunoblots using specific antibody.

(B) Interaction of FBXL6-FLAG with partners and substrates were analyzed in LTN1-KO (L), NEMF-KO (N), double LTN1/NEMF-KO (N/L), and control cells. FBXL6-FLAG or GFP (β-gal) were expressed in these different cells; IPs were performed using anti-FLAG; and interactions with MRPL45, SKP1, and HSPA1A were analyzed by immunoblots.

(C) Quantification of these interactions. Values represent protein levels normalized to FLAG pulled down and expressed as percentage of IP performed in control cells (n = 5–6, ***p < 0.001, **p < 0.01, *p < 0.05, one-way ANOVA, Holm-Sidak test).

(D) Localization of FBXL6-FLAG was analyzed in control (ctrl), NEMF-KO (N-KO), LTN1-KO (L-KO), and NEMF/LTN1 double-KO (N/L-KO) cells by immunofluorescence. Mitochondria and FBXL6 were labeled using anti-TOM20 (green) and anti-FLAG (red) respectively. Nucleus was stained with DAPI (blue).

(E) Quantification of cell number containing cytosolic FBXL6 (gray bars) or GFP (white bars) clusters. GFP distribution is represented in Figure S6B (n = 3, >150 cells per n, *p < 0.05, ***p < 0.001, ordinary one-way ANOVA, Holm-Sidak test).

(F) Control cells (WT) or NEMF-KO (N-KO) expressing MRPL45-HA-NS were transfected with FBXL6-FLAG (or control) and treated with epoxomicin for 0, 4, or 8 h. Relative accumulation of MRPL45 over the time was measured using anti-HA and normalized to actin (n = 3).

MRPL45-NS upon epoxomicin treatment was strongly reduced in NEMF-KO, but this effect was reversed by expression of FBXL6 (Figure 5F). Taken together, these results demonstrated that the NEMF-dependent sensing of the 60S obstruction is not necessary for the FBXL6-dependent mechanism, but this sensing participates in the activation and facilitates the FBXL6 action by enhancing interactions with its substrate.

As we reported above, FBXL6 also interacts with many chaperones, including HSPA1A, which plays an important role in quality control of nascent and newly synthesized proteins[7,33] and physically interacts with the translating ribosome.[34] Thus, we analyzed the role of this chaperone in the FBXL6-dependent mechanism. Using a blue native polyacrylamide gel electrophoresis (BN-PAGE) approach performed on a whole-cell extract, we observed buildup of MRPL45 in FBXL6-KO cells under the form of aggregates, and these forms were absent in control cells (Figures 6A and 6B). We found that these aggregates comigrated with HSPA1A. HSPA1A/MRPL45 aggregates were found at a lower molecular weight in FBXL4-KO cells, confirming the involvement of FBXL4 in mitochondrial proteostasis, whereas FBXL4 did not interact with MRPL45 (Figure 6C). The different size of HSPA1A aggregates observed in FBXL4- and

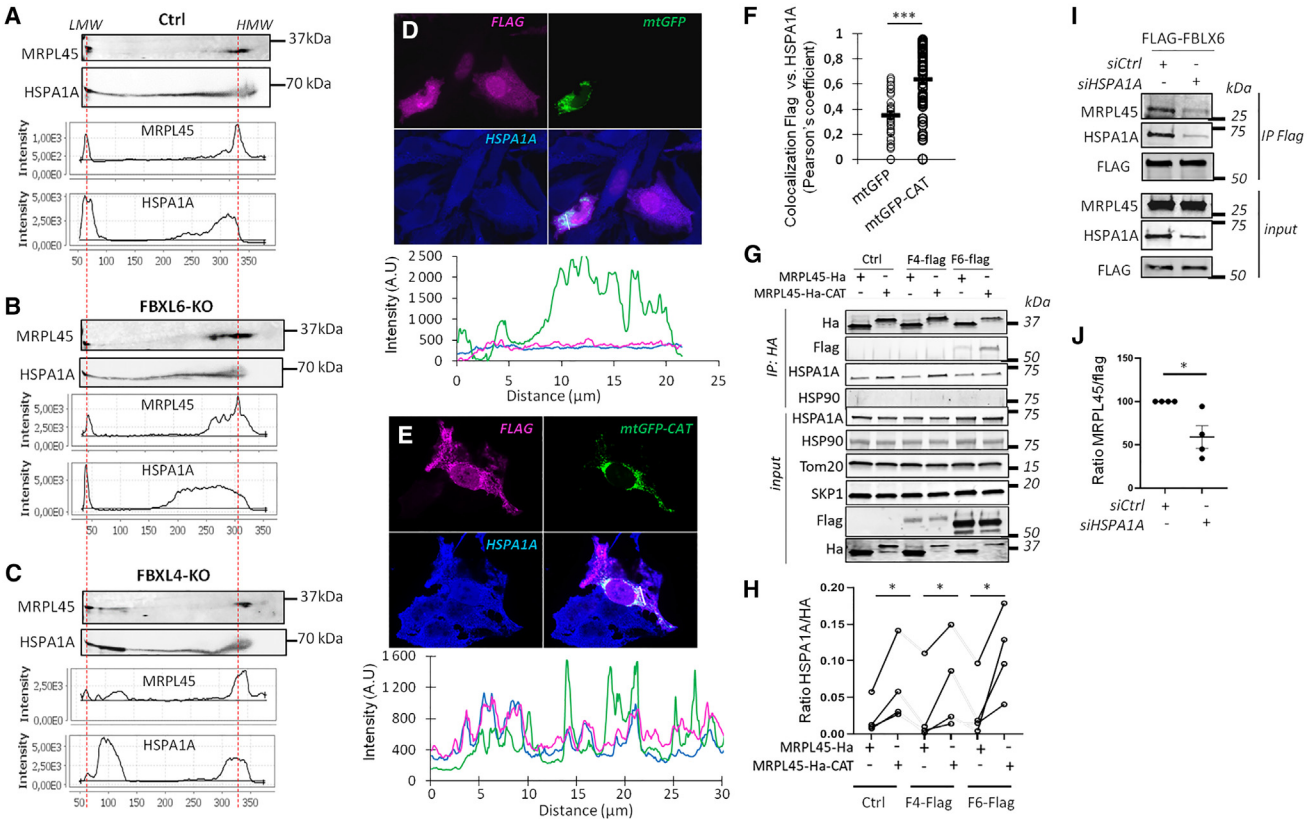

Figure 6. HSPA1A is involved in an FBXL6-dependent mechanism

(A–C) BN-PAGE was performed on whole-cell extracts from control cells (A), FBXL6-KO (B), or FBXL4-KO (C) and control cells. Aggregates of mitochondrial ribosomal proteins and chaperones were studied using anti-mitochondrial ribosomal protein L45 (MRPL45) and anti-heat shock protein 1A1 (HSP1A1) antibodies. Plots display the quantification of the different profiles and red lines indicate free MRPL45 at the low-molecular-weight (LMW) side and the native mitochondrial ribosome at the high-molecular-weight (HMW) side.

(D and E) Colocalization of FBXL6-FLAG and HSPA1A was assayed by immunofluorescence in presence of WT mitochondrial GFP (mitoGFP; D) or CAT-tailed mitochondrial GFP (mtGFP-CAT; E). FBXL6 and HSPA1A were labeled with anti-FLAG (red) and anti-HSPA1A (blue). Line scales show the recruitment of FBXL6 and HSPA1A to mtGFP-CAT aggregates.

(F) HSPA1A and FBXL6 colocalization was quantified by measuring the Pearson's correlation coefficient in the presence of mtGFP or mtGFP-CAT. Each dot is the value for one cell (n = 3, ***p < 0.001, unpaired t test).

(G and H) Cells expressing FBXL4-FLAG, FBXL6, or control cells were transfected with WT MRPL45- or MRPL45-HA-CAT. HA or FLAG IP was performed and the immunoprecipitated proteins were analyzed using immunoblots (G). Quantification of HSPA1A pulled down with HA expressed as HSPA1A/HA band ratio (H; n = 4, *p < 0.05, paired t test).

(I and J) HSPA1A was downregulation by using small interfering RNA (siRNA) in cells expressing FBXL6-FLAG and FLAG IP was performed (I). Binding of MRPL45 was analyzed by immunoblots and relative level was normalized to FLAG (J; n = 4, *p < 0.05, unpaired t test).

FBXL6-KO cells also pointed out discrepancies between related mechanisms. To test if these aggregates could be triggered by defective translation of mitochondrial proteins, we analyzed the subcellular localization of HSPA1A in the presence of CAT-tailed mtGFP. Upon expression of control mtGFP, HSPA1A displayed a diffused cellular localization (Figure 6D), while expression of the CAT-tailed mtGFP induced the relocalization of HSPA1A to precise cytosolic foci (Figure 6E). We found that expression of the CAT-tailed mtGFP led to the translocation of FBXL6 to these sites containing HSPA1 and the defective mitochondrial GFP (Figures 6E–6F, line scales). Increased colocalization between HSPA1A and FBXL6 in the presence of CAT-tailed mtGFP was confirmed by high Pearson's colocalization factor (Figure 6F). Furthermore, IPs of CAT-tailed versus WT MRPL45 revealed that HSPA1A had preferential interactions with the defective form of the ribosomal protein (Figures 6G and 6H). However, HSPA1A/MRPL45-CAT interactions were not significantly modulated by the exogenous expression of either FBXL4 or FBXL6 (Figure 6H). Finally, we found that silencing of HSPA1A dramatically reduced the ability of FBXL6 to bind MRPL45 (Figures 6I and 6J). Taken together, these results demonstrate that HSPA1A carries defective ribosomal proteins to FBXL6.

DISCUSSION

In the current study, we investigate the function of FBXL6, a cytosolic E3 ubiquitin ligase. We uncover that this E3 participates in the quality control of newly synthesized proteins, including

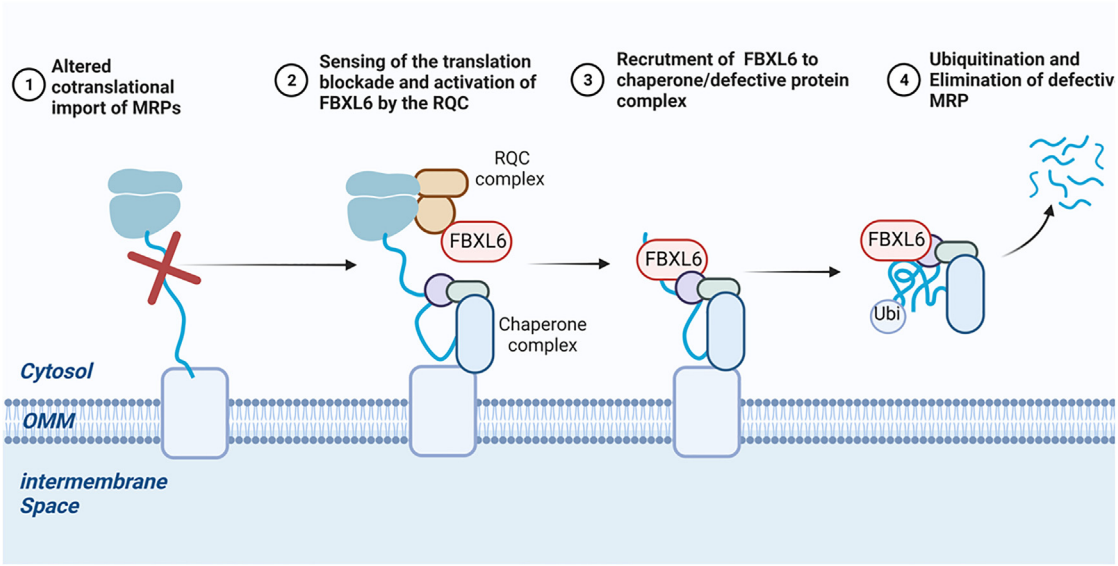

Figure 7. Model of FBXL6-dependent mechanism

Defective cotranslational import (1) of mitochondrial ribosomal proteins (MRPs) leads to the activation of the RQC and the folding stress responses (2). The RQC machinery induces the recruitment of FBXL6 to the mis/unfolded MRP and the chaperone complex (3) and the defective is ubiquitinated (4).

certain mitochondrial ribosomal proteins. Our results indicate that FBXL6 contributes to eliminating defective proteins through a mechanism involving RQC players and HSPs required for the homeostasis of newly synthesized proteins (Figure 7). Impairments of the FBXL6-dependent mechanism lead to mitochondrial metabolic dysfunctions.

FBXL6, an element of the mitoRQC in mammalian cells

By investigating the role played by Vms1, Izawa and colleagues revealed a straddling mechanism, the mitoRQC, that unified the quality control associated with the cytosolic translation and the mitochondrial import in yeast.[15] Complementing these findings, it was shown that the UBX domain-containing protein 2 (Ubx2) directly interacts with the TOM complex and recruits Cdc48 to tag defective newly synthesized proteins for proteasomal degradation.[35] Such a mechanism has not yet been described in higher eukaryotes, but its existence is highly probable. Indeed, Wu et al. have demonstrated in *Drosophila* that mitochondrial damage induced ribosome stalling at the OMM, which promotes the recruitment of PELO and ABCE1 at these sites.[17] Notably, it was recently proposed that loss-of-function mutations in the gene coding for ANKFZ1, the mammalian homolog of Vms1, are responsible for infantile-onset inflammatory bowel disease, and patients' cells carrying these mutations exhibit deregulation of mitochondrial integrity.[19] In this study, the authors also reported that ANKZF1 translocates to the mitochondria under oxidative stress.[19]

Using mammalian cell models, we have established the molecular bases of the mechanism that acts at the interface between the cytosolic translation and the mitochondria to eliminate aberrant defective mitochondrial proteins in the early step of their lifespan. We have found that FBXL6 binds newly synthesized mitochondrial ribosomal proteins, and cells with FBXL6 deleted fail to eliminate aberrant proteins, which imitates translational defects such as ribosomal mitochondrial proteins carrying a CAT tail or lacking a stop codon. In addition, FBXL6 interacts with keys actors of RQC, such as ZNF598, PELO, and NEMF,[18,36] and chaperones involved in the folding and transport of newly synthesized polypeptides (HSPA1A, HSPA4, and HSP90AB1) or in the sorting and the delivery of nascent/newly synthesized proteins at the OMM (HSPA8, HSP90AA1).[6] Notably, knockdown of NEMF or HSPA1A hamper the ability of FBXL6 to bind its substrates, showing that these processes play a preponderant role in triggering the FBXL6-dependent mechanism. Our results indicate that this FBXL6-dependent quality control plays an important role in mitochondrial functions since its deletion reduces mitochondrial metabolic activity and it renders the organelle more sensible to proteostatic stress. Thus, our results support that FBXL6 participates in the mammalian equivalent of the mitoRQC.

Contribution of E3 ubiquitin ligases to the mitoRQC

During the process of protein quality control, E3 ubiquitin ligases play a central role as they recognize and label proteins that need to be degraded, and, therefore, these enzymes provide the specificity of the RQC response. Mammalian cells contain approximately 6-fold more E3 ubiquitin ligases than yeast, and this discrepancy suggests a higher specificity regarding substrate recognition or/and physiological regulation.[37,38] In yeast, Duttler et al. showed that ubiquitination during translation affects up to 5% of nascent proteins, and they demonstrated that these modifications are carried out by several E3 ubiquitin ligases.[12] Some of them promote the degradation of non-stop protein (Ltn1) or nascent unfolded proteins (Hul5, Hrd1). In mammalian cells, Joazeiro's group has recently found that $CRL2^{KLHDC10}$ and Pirh2 can eliminate defective newly synthesized proteins in

the absence of LTN1 and in an NEMF-dependent manner.[39] Therefore, they demonstrate that LTN1 is not the only E3 involved in RQC in mammalian cells.

In this line, the role played by other E3s in the mitoRQC process has also emerged lately. Indeed, Wu and colleagues have showed that the collapse of the mitochondrial membrane potential induces cytosolic ribosome stalling.[17] In this condition, ABCE1, a protein involved in the splitting of the ribosomal subunits, is ubiquitinated by NOT4 and accumulated at the mitochondrial surface to trigger mitophagy mediated by the PINK1 pathway. In this line, MARCH5 is an OMM-located E3 ubiquitin ligase previously reported to regulate mitochondrial morphology.[40] It was recently demonstrated that this enzyme orchestrates the cytosolic retention of newly synthesized proteins by promoting their ubiquitination and their consecutive proteasomal degradation.[41] Interestingly, these authors propose that other E3s ubiquitinate proteins before their import since MARCH5 knockdown does not fully eliminate newly synthesized mitochondrial protein ubiquitination. Participation depends on the physiological context, such as the preferential recognition of substrates (e.g., FBXL6), the responses to physiological stimuli (e.g., NOT4), or tissue specificity.

Limitations of the study

Although our study provides a comprehensive view of the molecular bases of the FBXL6-dependent mechanism, we still need to understand how FBXL6 recognizes specifically defective ribosomal proteins, and this is one of the most challenging questions. Thrun et al. reported that $CRL2^{KLHDC10}$ and Pirh2 recognize the CAT tail of defective proteins.[39] In our study, we demonstrate that CAT tails are not per se the signal that FBXL6 recognized to catalyze the protein degradation. In fact, FBXL6 affects the degradation of MRPLs-CAT but not SDHA-CAT. On the other hand, FBXL6 has specificity for both cytosolic and mitochondrial ribosomal proteins, which exclude recognition of the mitochondrial leading sequences. This specificity could be provided by partners such as specific HSPs proteins that connect the SCF^{FBXL6} complex to aberrant ribosomal proteins. Nevertheless, we cannot exclude the presence of a specific degron in unfolded ribosomal proteins.

STAR★METHODS

Detailed methods are provided in the online version of this paper and include the following:

- KEY RESOURCES TABLE
- RESOURCE AVAILABILITY
  - Lead contact
  - Materials availability
  - Data and code availability
- EXPERIMENTAL MODEL AND SUBJECT PARTICIPANT DETAILS
- METHOD DETAILS
  - Cell lines, culture conditions, and transfections
  - *In vitro* cell growth assay
  - Generation of control, FBXL4-, and FBXL6-KO cells
  - Generation of GFP, FBXL4, and FBXL6 turboID cells
  - Analysis of gene expression by quantitative PCR
  - Plasmid construction
  - Cell fractionation and trypsin accessibility assay
  - Immunoblots
  - BN-PAGE
  - Immunoprecipitation
  - Proteome analyses by mass spectrometry
  - Pulsed SILAC assay
  - Turbo ID and mass spectrometry analysis
  - Immunofluorescence microscopy
  - Oxygen consumption analyses and ATP measurement
  - Cell cycle assays
  - Graphical methods
- QUANTIFICATION AND STATISTICAL ANALYSIS

SUPPLEMENTAL INFORMATION

Supplemental information can be found online at https://doi.org/10.1016/j.celrep.2023.112579.

ACKNOWLEDGMENTS

G.B.'s salary is supported by the Centre National de la Recherche Scientifique (CNRS). He was supported by the Agence National de la Recherche (ANR) (n°ANR-17-CE14-0039-01), by Région Nouvelle-Aquitaine (2019-1R30124), and by AFM (AFM-24061). R.P.N. and A.-M.D. were supported by an ANR grant (ANR-18-CE12-0021-01 "Polyglot") and by the French National Program Investissement d'Avenir (Labex MitoCross). We thank Angela Sequiera for technical support. We acknowledge Johana Chicher from the Plateforme Protéomique Strasbourg Esplanade (CNRS) for performing the TurboID mass-spectrometry analysis. We thank Dr. Claudio Joazeiro for LTN1, NEMF, and LTN1/NEMF-KO cells.

AUTHOR CONTRIBUTIONS

J.L. and G.B. conceived the study. J.L., C.L., W.M., A.A.C., H.R., and G.B. performed the biochemical experiments. J.L., C.L., and R.P.N. designed and conceived genetic constructs. J.-W.D. and A.A. performed the mass spectrometry analyses. W.M. and H.R. performed the cell cycle assays. R.P.N. and A.-M.D. generated HCT116 TurboID cells and performed the proximity labeling assays. G.B. wrote the manuscript with contributions from all authors.

DECLARATION OF INTERESTS

The authors declare no competing interests.

Received: December 21, 2022
Revised: April 3, 2023
Accepted: May 15, 2023
Published: June 1, 2023

REFERENCES

1. Rath, S., Sharma, R., Gupta, R., Ast, T., Chan, C., Durham, T.J., Goodman, R.P., Grabarek, Z., Haas, M.E., Hung, W.H.W., et al. (2021). MitoCarta3.0: an updated mitochondrial proteome now with sub-organelle localization and pathway annotations. Nucleic Acids Res. *49*, D1541–D1547. https://doi.org/10.1093/nar/gkaa1011.
2. Kellems, R.E., and Butow, R.A. (1974). Cytoplasmic type 80 S ribosomes associated with yeast mitochondria. J. Biol. Chem. *249*, 3304–3310. https://doi.org/10.1016/s0021-9258(19)42673-2.
3. Gold, V.A., Chroscicki, P., Bragoszewski, P., and Chacinska, A. (2017). Visualization of cytosolic ribosomes on the surface of mitochondria by

electron cryo-tomography. EMBO Rep. *18*, 1786–1800. https://doi.org/10.15252/embr.201744261.

4. Lesnik, C., Cohen, Y., Atir-Lande, A., Schuldiner, M., and Arava, Y. (2014). OM14 is a mitochondrial receptor for cytosolic ribosomes that supports co-translational import into mitochondria. Nat. Commun. *5*, 5711. https://doi.org/10.1038/ncomms6711.

5. Lazarou, M., Jin, S.M., Kane, L.A., and Youle, R.J. (2012). Role of PINK1 binding to the TOM complex and alternate intracellular membranes in recruitment and activation of the E3 ligase parkin. Dev. Cell *22*, 320–333. https://doi.org/10.1016/j.devcel.2011.12.014.

6. Young, J.C., Hoogenraad, N.J., and Hartl, F.U. (2005). Molecular chaperones Hsp90 and Hsp70 deliver preproteins to the mitochondrial import receptor Tom70. Cell *112*, 41–50. https://doi.org/10.1016/s0968-0004(05)00043-5.

7. Tian, G., Hu, C., Yun, Y., Yang, W., Dubiel, W., Cheng, Y., and Wolf, D.A. (2021). Dual roles of HSP70 chaperone HSPA1 in quality control of nascent and newly synthesized proteins. EMBO J. *40*, e106183. https://doi.org/10.15252/embj.2020106183.

8. Mohanraj, K., Wasilewski, M., Benincá, C., Cysewski, D., Poznanski, J., Sakowska, P., Bugajska, Z., Deckers, M., Dennerlein, S., Fernandez-Vizarra, E., et al. (2019). Inhibition of proteasome rescues a pathogenic variant of respiratory chain assembly factor COA7. EMBO Mol. Med. *11*, 1–21. https://doi.org/10.15252/emmm.201809561.

9. Boos, F., Krämer, L., Groh, C., Jung, F., Haberkant, P., Stein, F., Wollweber, F., Gackstatter, A., Zöller, E., van der Laan, M., et al. (2019). Mitochondrial protein-induced stress triggers a global adaptive transcriptional programme. Nat. Cell Biol. *21*, 442–451. https://doi.org/10.1038/s41556-019-0294-5.

10. Wrobel, L., Topf, U., Bragoszewski, P., Wiese, S., Sztolsztener, M.E., Oeljeklaus, S., Varabyova, A., Lirski, M., Chroscicki, P., Mroczek, S., et al. (2015). Mistargeted mitochondrial proteins activate a proteostatic response in the cytosol. Nature *524*, 485–488. https://doi.org/10.1038/nature14951.

11. Pechmann, S., Willmund, F., and Frydman, J. (2013). The ribosome as a hub for protein quality control. Mol. Cell *49*, 411–421. https://doi.org/10.1016/j.molcel.2013.01.020.

12. Duttler, S., Pechmann, S., and Frydman, J. (2013). Principles of cotranslational ubiquitination and quality control at the ribosome. Mol. Cell *50*, 379–393. https://doi.org/10.1016/j.molcel.2013.03.010.

13. Joazeiro, C.A.P. (2019). Mechanisms and functions of ribosome-associated protein quality control. Nat. Rev. Mol. Cell Biol. *20*, 368–383. https://doi.org/10.1038/s41580-019-0118-2.

14. Bengtson, M.H., and Joazeiro, C.A.P. (2010). Role of a ribosome-associated E3 ubiquitin ligase in protein quality control. Nature *467*, 470–473. https://doi.org/10.1038/nature09371.

15. Izawa, T., Park, S.H., Zhao, L., Hartl, F.U., and Neupert, W. (2017). Cytosolic protein Vms1 links ribosome quality control to mitochondrial and cellular homeostasis. Cell *171*, 890–903.e18. https://doi.org/10.1016/j.cell.2017.10.002.

16. Heo, J.M., Livnat-Levanon, N., Taylor, E.B., Jones, K.T., Dephoure, N., Ring, J., Xie, J., Brodsky, J.L., Madeo, F., Gygi, S.P., et al. (2010). A stress-responsive system for mitochondrial protein degradation. Mol. Cell *40*, 465–480. https://doi.org/10.1016/j.molcel.2010.10.021.

17. Wu, Z., Wang, Y., Lim, J., Liu, B., Li, Y., Vartak, R., Stankiewicz, T., Montgomery, S., and Lu, B. (2018). Ubiquitination of ABCE1 by NOT4 in response to mitochondrial damage links Co-translational quality control to PINK1-directed mitophagy. Cell Metab. *28*, 130–144.e7. https://doi.org/10.1016/j.cmet.2018.05.007.

18. Pisareva, V.P., Skabkin, M.A., Hellen, C.U.T., Pestova, T.V., and Pisarev, A.V. (2011). Dissociation by Pelota, Hbs1 and ABCE1 of mammalian vacant 80S ribosomes and stalled elongation complexes. EMBO J. *30*, 1804–1817. https://doi.org/10.1038/emboj.2011.93.

19. Van Haaften-Visser, D.Y., Harakalova, M., Mocholi, E., Van Montfrans, J.M., Elkadri, A., Rieter, E., Fiedler, K., Van Hasselt, P.M., Triffaux, E.M.M., Van Haelst, M.M., et al. (2017). Ankyrin repeat and zinc-finger domain-containing 1 mutations are associated with infantile-onset inflammatory bowel disease. J. Biol. Chem. *292*, 7904–7920. https://doi.org/10.1074/jbc.M116.772038.

20. Gai, X., Ghezzi, D., Johnson, M.A., Biagosch, C.A., Shamseldin, H.E., Haack, T.B., Reyes, A., Tsukikawa, M., Sheldon, C.A., Srinivasan, S., et al. (2013). Mutations in FBXL4, encoding a mitochondrial protein, cause early-onset mitochondrial encephalomyopathy. Am. J. Hum. Genet. *93*, 482–495. https://doi.org/10.1016/j.ajhg.2013.07.016.

21. Bonnen, P.E., Yarham, J.W., Besse, A., Wu, P., Faqeih, E.A., Al-Asmari, A.M., Saleh, M.A.M., Eyaid, W., Hadeel, A., He, L., et al. (2013). Mutations in FBXL4 cause mitochondrial encephalopathy and a disorder of mitochondrial DNA maintenance. Am. J. Hum. Genet. *93*, 471–481. https://doi.org/10.1016/j.ajhg.2013.07.017.

22. Huemer, M., Karall, D., Schossig, A., Abdenur, J.E., Al Jasmi, F., Biagosch, C., Distelmaier, F., Freisinger, P., Graham, B.H., Haack, T.B., et al. (2015). Clinical, morphological, biochemical, imaging and outcome parameters in 21 individuals with mitochondrial maintenance defect related to FBXL4 mutations. J. Inherit. Metab. Dis. *38*, 905–914. https://doi.org/10.1007/s10545-015-9836-6.

23. Reitzer, L.J., Wice, B.M., and Kennell, D. (1979). Evidence that glutamine, not sugar, is the major energy source for cultured HeLa cells. J. Biol. Chem. *254*, 2669–2676. https://doi.org/10.1016/s0021-9258(17)30124-2.

24. Melser, S., Chatelain, E.H., Lavie, J., Mahfouf, W., Jose, C., Obre, E., Goorden, S., Priault, M., Elgersma, Y., Rezvani, H.R., et al. (2013). Rheb regulates mitophagy induced by mitochondrial energetic status. Cell Metab. *17*, 719–730. https://doi.org/10.1016/j.cmet.2013.03.014.

25. Hirano, A., Yumimoto, K., Tsunematsu, R., Matsumoto, M., Oyama, M., Kozuka-Hata, H., Nakagawa, T., Lanjakornsiripan, D., Nakayama, K.I., and Fukada, Y. (2013). FBXL21 regulates oscillation of the circadian clock through ubiquitination and stabilization of cryptochromes. Cell *152*, 1106–1118. https://doi.org/10.1016/j.cell.2013.01.054.

26. Shao, S., Brown, A., Santhanam, B., and Hegde, R.S. (2015). Structure and assembly pathway of the ribosome quality control complex. Mol. Cell *57*, 433–444. https://doi.org/10.1016/j.molcel.2014.12.015.

27. Branon, T.C., Bosch, J.A., Sanchez, A.D., Udeshi, N.D., Svinkina, T., Carr, S.A., Feldman, J.L., Perrimon, N., and Ting, A.Y. (2018). Efficient proximity labeling in living cells and organisms with TurboID. Nat. Biotechnol. *36*, 880–887. https://doi.org/10.1038/nbt.4201.

28. Mason, B., and Laman, H. (2020). The FBXL family of F-box proteins: variations on a theme: the FBXL family of F-box proteins. Open Biol. *10*, 200319. https://doi.org/10.1098/rsob.200319.

29. Sabouny, R., Wong, R., Lee-Glover, L., Greenway, S.C., Sinasac, D.S., Care4Rare Canada; Khan, A., and Shutt, T.E. (2019). Characterization of the C584R variant in the mtDNA depletion syndrome gene FBXL4, reveals a novel role for FBXL4 as a regulator of mitochondrial fusion. Biochim. Biophys. Acta Mol. Basis Dis. *1865*, 165536. https://doi.org/10.1016/j.bbadis.2019.165536.

30. Ansar, M., Paracha, S.A., Serretti, A., Sarwar, M.T., Khan, J., Ranza, E., Falconnet, E., Iwaszkiewicz, J., Shah, S.F., Qaisar, A.A., et al. (2019). Biallelic variants in FBXL3 cause intellectual disability, delayed motor development and short stature. Hum. Mol. Genet. *28*, 972–979. https://doi.org/10.1093/hmg/ddy406.

31. Shen, P.S., Park, J., Qin, Y., Li, X., Parsawar, K., Larson, M.H., Cox, J., Cheng, Y., Lambowitz, A.M., Weissman, J.S., et al. (2015). Rqc2p and 60S ribosomal subunits mediate mRNA-independent elongation of nascent chains. Science *347*, 75–78. https://doi.org/10.1126/science.1259724.

32. Kostova, K.K., Hickey, K.L., Osuna, B.A., Hussmann, J.A., Frost, A., Weinberg, D.E., and Weissman, J.S. (2017). CAT-tailing as a fail-safe mechanism for efficient degradation of stalled nascent polypeptides. Science *357*, 414–417. https://doi.org/10.1126/science.aam7787.

33. Hartl, F.U., and Hayer-Hartl, M. (2002). Protein folding. Molecular chaperones in the cytosol: from nascent chain to folded protein. Science *295*, 1852–1858. https://doi.org/10.1126/science.1068408.

34. Jaiswal, H., Conz, C., Otto, H., Wölfle, T., Fitzke, E., Mayer, M.P., and Rospert, S. (2011). The chaperone network connected to human ribosome-associated complex. Mol. Cell Biol. *31*, 1160–1173. https://doi.org/10.1128/mcb.00986-10.

35. Mårtensson, C.U., Priesnitz, C., Song, J., Ellenrieder, L., Doan, K.N., Boos, F., Floerchinger, A., Zufall, N., Oeljeklaus, S., Warscheid, B., et al. (2019). Mitochondrial protein translocation-associated degradation. Nature *569*, 679–683. https://doi.org/10.1038/s41586-019-1227-y.

36. Sundaramoorthy, E., Leonard, M., Mak, R., Liao, J., Fulzele, A., and Bennett, E.J. (2017). ZNF598 and RACK1 regulate mammalian ribosome-associated quality control function by mediating regulatory 40S ribosomal ubiquitylation. Mol. Cell *65*, 751–760.e4. https://doi.org/10.1016/j.molcel.2016.12.026.

37. Li, W., Bengtson, M.H., Ulbrich, A., Matsuda, A., Reddy, V.A., Orth, A., Chanda, S.K., Batalov, S., and Joazeiro, C.A.P. (2008). Genome-wide and functional annotation of human E3 ubiquitin ligases identifies MULAN, a mitochondrial E3 that regulates the organelle's dynamics and signaling. PLoS One *3*, e1487. https://doi.org/10.1371/journal.pone.0001487.

38. Finley, D., Ulrich, H.D., Sommer, T., and Kaiser, P. (2012). The ubiquitin-proteasome system of Saccharomyces cerevisiae. Genetics *192*, 319–360. https://doi.org/10.1534/genetics.112.140467.

39. Thrun, A., Garzia, A., Kigoshi-Tansho, Y., Patil, P.R., Umbaugh, C.S., Dallinger, T., Liu, J., Kreger, S., Patrizi, A., Cox, G.A., et al. (2021). Convergence of mammalian RQC and C-end rule proteolytic pathways via alanine tailing. Mol. Cell *81*, 2112–2122.e7. https://doi.org/10.1016/j.molcel.2021.03.004.

40. Karbowski, M., Neutzner, A., and Youle, R.J. (2007). The mitochondrial E3 ubiquitin ligase MARCH5 is required for Drp1 dependent mitochondrial division. J. Cell Biol. *178*, 71–84. https://doi.org/10.1083/jcb.200611064.

41. Phu, L., Rose, C.M., Tea, J.S., Wall, C.E., Verschueren, E., Cheung, T.K., Kirkpatrick, D.S., and Bingol, B. (2020). Dynamic regulation of mitochondrial import by the ubiquitin system. Mol. Cell *77*, 1107–1123.e10. https://doi.org/10.1016/j.molcel.2020.02.012.

42. Huang, D.W., Sherman, B.T., and Lempicki, R.A. (2009). Systematic and integrative analysis of large gene lists using DAVID bioinformatics resources. Nat. Protoc. *4*, 44–57. https://doi.org/10.1038/nprot.2008.211.

43. Deutsch, E.W., Bandeira, N., Sharma, V., Perez-Riverol, Y., Carver, J.J., Kundu, D.J., García-Seisdedos, D., Jarnuczak, A.F., Hewapathirana, S., Pullman, B.S., et al. (2020). The ProteomeXchange consortium in 2020: enabling "big data" approaches in proteomics. Nucleic Acids Res. *48*, D1145–D1152. https://doi.org/10.1093/nar/gkz984.

44. Bouyssié, D., Hesse, A.M., Mouton-Barbosa, E., Rompais, M., MacRon, C., Carapito, C., Gonzalez De Peredo, A., Couté, Y., Dupierris, V., Burel, A., et al. (2020). Proline: an efficient and user-friendly software suite for large-scale proteomics. Bioinformatics *36*, 3148–3155. https://doi.org/10.1093/bioinformatics/btaa118.

45. Henriet, E., Abou Hammoud, A., Dupuy, J.W., Dartigues, B., Ezzoukry, Z., Dugot-Senant, N., Leste-Lasserre, T., Pallares-Lupon, N., Nikolski, M., Le Bail, B., et al. (2017). Argininosuccinate synthase 1 (ASS1): a marker of unclassified hepatocellular adenoma and high bleeding risk. Hepatology *66*, 2016–2028. https://doi.org/10.1002/hep.29336.

46. Ong, S.E., and Mann, M. (2006). A practical recipe for stable isotope labeling by amino acids in cell culture (SILAC). Nat. Protoc. *1*, 2650–2660. https://doi.org/10.1038/nprot.2006.427.

47. Robin, T., Bairoch, A., Müller, M., Lisacek, F., and Lane, L. (2019). Correction to: large-scale reanalysis of publicly available hela cell proteomics data in the context of the human proteome project. J. Proteome Res. *18*, 1926–1927. https://doi.org/10.1021/acs.jproteome.9b00113.

48. Lavado-García, J., Jorge, I., Cervera, L., Vázquez, J., and Gòdia, F. (2020). Multiplexed quantitative proteomic analysis of HEK293 provides insights into molecular changes associated with the cell density effect, transient transfection, and virus-like particle production. J. Proteome Res. *19*, 1085–1099. https://doi.org/10.1021/acs.jproteome.9b00601.

STAR★METHODS

KEY RESOURCES TABLE

REAGENT or RESOURCE	SOURCE	IDENTIFIER
Antibodies		
Mouse Anti-ATP5A mAb	Santa Cruz Biotech	Cat# sc-136178; RRID:AB_2061764
Mouse anti-beta-Actin mAb	Sigma Aldrich	Cat# A1978; RRID:AB_476692
Mouse anti-MT-CO2 mAb	Santa Cruz Biotech	Cat# sc-514489
Mouse anti-COX4 mAb	Santa Cruz Biotech	Cat# sc-376731
Mouse anti-FLAG M2 mAb	Sigma-Aldrich	Cat# F3165; RRID:AB_259529
Rabbit anti-FBXL4 pAb	Invitrogen	Custom antibody AB2862
Rabbit anti-FBXL6 pAb	Invitrogen	Custom antibody AB2863/AB2864
Mouse anti-GFP mAb	Roche	Cat# 11814460001; RRID:AB_390913
Rabbit anti-GAPDH pAb	Santa Cruz Biotech	Cat# sc-25778; RRID:AB_10167668
Rabbit anti-HA mAb	Cell Signaling	Cat# 3724; RRID:AB_1549585
Mouse anti-HSP60	Novus	Cat# NBP2-22440
Rabbit anti-HSP90 mAb	Cell Signaling	Cat# 4877; RRID:AB_2233307
Rabbit anti-HSPA1A pAb	ThermoFisher	Cat# PA5-28003; RRID:AB_2545479
Rabbit anti-RNF160 pAb	Proteintech	Cat# PR-28452-1-AP
Rabbit anti-MRPL42	Novus	Cat# NBP1-83171; RRID:AB_11006589
Rabbit anti-MRPL45	Novus	Cat# NBP1-82764; RRID:AB_11019553
Mouse anti-MRPS34	Novus	Cat# NBP2-45432
Mouse anti-Myc tag mAb	Merck Millipore	Cat# 05–419; RRID:AB_309725
Rabbit Anti-Nemf	Bethyl Laboratories	Cat# A305-758A-M
Mouse anti-NDUFS3 mAb	Santa Cruz Biotech	Cat# sc-374282; RRID:AB_10991315
Mouse anti-OPA-1 mAb	BD Biosciences	Cat# 612607; RRID:AB_399889
Rabbit anti PELO	GeneTex	Cat# GTX120446
Rabbit anti-RPL9	Novus	Cat# NBP1-82853; RRID:AB_11027189
Mouse anti-SDHA mAb	Santa Cruz Biotech	Cat# sc-166909; RRID:AB_10611174
Mouse anti-SKP1	Novus	Cat# NBP2-37539
Rabbit anti-Tom20 (FL-145) pAb	Santa Cruz Biotech	Cat# sc-11415; RRID:AB_2207533
Rabbit anti-UQCRC2 pAb	Proteintech	Cat# 14742-1-AP; RRID:AB_2241442
Mouse anti-V5-Tag mAb	Biorad	Cat# MCA1360; RRID:AB_322378
Rabbit anti-ZNF598	GeneTex	Cat# GTX119245
IRDye 800CW Donkey anti-Mouse IgG antibody	LI-COR Biosciences	Cat# 926–32212; RRID:AB_621847
IRDye 800CW Goat anti-Rabbit IgG antibody	LI-COR Biosciences	Cat# 926–32211; RRID:AB_621843
IRDye 680RD Donkey anti-Mouse IgG antibody	LI-COR Biosciences	Cat# 926–68072; RRID:AB_10953628
IRDye 680RD Donkey anti-Rabbit IgG antibody	LI-COR Biosciences	Cat# 926–68073; RRID:AB_10954442
Goat Anti-Mouse IgG (H L)-HRP Conjugate antibody	Bio-Rad	Cat# 170–6516; RRID:AB_11125547
Goat Anti-Rabbit IgG (H L)-HRP Conjugate antibody	Bio-Rad	Cat# 170–6515; RRID:AB_11125142
Goat anti-Mouse IgG (H + L) Cross-Adsorbed Secondary Antibody, Alexa Fluor 350	Thermo Fisher Scientific	Cat# A-11045; RRID:AB_2534100
Goat anti-Rabbit IgG (H + L) Cross-Adsorbed Secondary Antibody, Alexa Fluor 350	Thermo Fisher Scientific	Cat# A-11046; RRID:AB_2534101
Goat anti-Mouse IgG (H + L) Cross-Adsorbed Secondary Antibody, Alexa Fluor 488	Thermo Fisher Scientific	Cat# A-11001; RRID:AB_2534069
Goat Anti-Rabbit IgG (H + L) Antibody, Alexa Fluor 488 Conjugated	Thermo Fisher Scientific	Cat# A-11008; RRID:AB_143165

(*Continued on next page*)

Continued

REAGENT or RESOURCE	SOURCE	IDENTIFIER
Goat anti-Mouse IgG (H + L) Cross-Adsorbed Secondary Antibody, Alexa Fluor 568	Thermo Fisher Scientific	Cat# A-11004; RRID:AB_2534072
Goat anti-Rabbit IgG (H + L) Cross-Adsorbed Secondary Antibody, Alexa Fluor 568	Thermo Fisher Scientific	Cat# A-11011; RRID:AB_143157
Goat anti-Mouse IgG (H + L) Cross-Adsorbed Secondary Antibody, Alexa Fluor 647	Thermo Fisher Scientific	Cat# A-21235; RRID:AB_2535804
Goat anti-Rabbit IgG (H + L) Cross-Adsorbed Secondary Antibody, Alexa Fluor 647	Thermo Fisher Scientific	Cat# A-21244; RRID:AB_2535812
Streptavidin Mag Sepharose®	Cytiva	Cat# 28-9857-38
Pierce™ Anti-HA Magnetic Beads	Thermo Fisher	Cat# 88836
Anti-FLAG® M2 Magnetic Beads	Sigma Aldrich	Cat# M8823
Chemicals, peptides, and recombinant proteins		
Epoxomycin	UBPBIO	Cat# F1400-5
Cycloheximide	Sigma-Aldrich	Cat# 01810
MG132	UBPBIO	Cat# F1101
Dithiothreitol	Sigma Aldrich	Cat# D5545
Protease Inhibitor Cocktail	Sigma-Aldrich	Cat# P8340
Bovine Serum Albumin	Sigma-Aldrich	Cat# A7906-500G
2-Mercaptoethanol	Sigma Aldrich	Cat# M3148
Digitonin	Sigma Aldrich	Cat# D141-100MG
Carfilzomib (PR-171)	UBPBio	Cat# F1300
Pierce™ BCA Protein Assay Kit	Thermo Scientific	Cat# 23225
Adenosine 5'-triphosphate disodium salt hydrate	Sigma Aldrich	Cat# A7699-5G
Critical commercial assays		
CellTiter-Glo® 2.0 Cell Viability Assay	Promega	Cat# G9242
Deposited data		
FBXL6 Knockdown cells proteome.	This study, ProteomeXchange	PXD037252
FBXL6 interacting proteome	This study, ProteomeXchange	PXD037248
FBXL6 interaction with newly synthesized proteins	This study, ProteomeXchange	PXD037602
biotinylated proteins in cells expressing GFP-TurboID	This study, ProteomeXchange	PXD027122
biotinylated proteins in cells expressing FBXL6-TurboID cells	This study, ProteomeXchange	PXD028161
Experimental models: Cell lines		
Wild-type HEK293	ATCC	Cat# CRL-1573; RRID: CVCL_0045
Wild-type HeLa cells	Sigma Aldrich	ECACC Cat# 93021013; RRID:CVCL_0030
FBXL4 KO HeLa stable	This manuscript	N/A
FBXL6 KO HeLa stable	This manuscript	N/A
HCT 116 cell line	ATCC	ATCC, CCL-247
TurboID FBXL4 HCT116 stable	This manuscript	N/A
TurboID FBXL6 HCT116 stable	This manuscript	N/A
Recombinant DNA		
pCMV-beta-galactosidase	Gift	N/A
pCMV6-AC-GFP	Origene	Cat# PS100010
FBXL3-Myc	Genscript	Clone ID: OHu06084C
FBXL4-Myc-DDK	Origene	Cat# RC208817
FBXL6-Myc-DDK	This paper	N/A
mlsFBXL4-GFP	This paper	N/A
mlsFBXL6-GFP	This paper	N/A
Cyto-GFP	This paper	N/A
Cyto-GFP-CAT	This paper	N/A

(*Continued on next page*)

Continued

REAGENT or RESOURCE	SOURCE	IDENTIFIER
Mito-GFP	This paper	N/A
Mito-GFP-CAT	This paper	N/A
MRPL45-HA-CAT	This paper	N/A
MRPL45-HA-NS	This paper	N/A
MRPL42-HA-CAT	This paper	N/A
MRPL42-HA-NS	This paper	N/A
SDHA-HA-CAT	This paper	N/A
SDHA-HA-NS	This paper	N/A
Software and algorithms		
graphpad Prism 9	Graphpad	N/A
DAVID 6.8	Huang et al.[42]	https://david.ncifcrf.gov
Other		
Biorender		Biorender.com
Fugene HD Transfection Reagent	Promega	Cat# E2311
RIPA buffer	Sigma-Aldrich	Cat# R0278
Laemmli Sample Buffer 4x	Bio-Rad	Cat# 1610747
Laemmli Sample Buffer 2×	Sigma Aldrich	Cat# S3401
Precision Plus Protein Dual Color Standards	Bio-Rad	Cat# 1610374
10x Tris/Glycine/SDS	Bio-Rad	Cat# 1610772
Mini-PROTEAN TGX Gels	Bio-Rad	Cat# 4561093
Mini-PROTEAN TGX gels IPG	Bio-Rad	Cat# 4561091
Trans-Blot Turbo RTA Midi 0.2 μm PVDF Transfer Kit	Bio-Rad	Cat# 1704273
Penicillin-Streptomycin	ThermoFisher Scientific	Cat# 15140122
DMEM, high glucose, GlutaMAX™ Supplement, pyruvate	ThermoFisher Scientific	Cat# 31966021
DMEM, no glucose	ThermoFisher Scientific	Cat# 11966025
HEPES (1M)	ThermoFisher Scientific	Cat# 15630056
L-Glutamine (200 mM)	ThermoFisher Scientific	Cat# 25030024
Sodium Pyruvate (100 mM)	ThermoFisher Scientific	Cat# 11360070
D-(+)-Galactose	Sigma Aldrich	Cat# G0625
Trypsin-EDTA (0.25%), phenol red	ThermoFisher Scientific	Cat# 25200072
SuperSignal™ West Pico PLUS	Thermo Scientific	Cat# 34577
SuperSignal™ West Femto	Thermo Scientific	Cat# 34095
Trypsin-EDTA (0.05%)	Gibco	Cat# 25300062
2-Mercaptoethanol	Sigma Aldrich	Cat# M3148
NativePAGE 20x running buffer	Invitrogen	Cat# BN2001

RESOURCE AVAILABILITY

Lead contact

Further information and requests for resources and reagents should be directed to and will be fulfilled by the lead contact, Giovanni Bénard (giovanni.benard@inserm.fr).

Materials availability

Plasmids generated in this study (please table above) will be shared upon request to the lead contact with a completed Materials Transfer Agreement.

This study did not generate new unique reagents.

Data and code availability

The mass spectrometry proteomics data have been deposited to the ProteomeXchange Consortium via the PRIDE partner repository.[42] Please refer to key resources table.

This paper does not report original code.
Any additional information required to reanalyze the data reported in this paper is available from the lead contact upon request.

EXPERIMENTAL MODEL AND SUBJECT PARTICIPANT DETAILS

HeLa were obtained from Merck and certified by the European Collection of Authenticated Cell Cultures (ECACC) and HEK cells from ATCC (CRL-1573). HCT116 cells were purchased from ATCC (CCL-247, ATCC). Cells were cultured in glucose media consisting of Dulbecco's modified Eagle medium (DMEM) medium containing 25 mM glucose. All media were supplemented with 10% heat-inactivated fetal bovine serum, 1 mM sodium pyruvate, MEM non-essential amino acids, 100 U/mL penicillin, and 100 μg/mL streptomycin. Cells were cultured in a 5% CO_2 atmosphere at 37°C and transfected using FugeneHD (Roche, Basel Switzerland) according to the manufacturer's protocol.

For experiments in the presence of different energy-related substrates, high-glucose medium was removed and replaced with DMEM glucose-free medium containing 10 mM galactose and supplemented with either 4 mM glutamine (glutamine media) or 5 mM glucose (glucose media). Cells were cultured for 48 h prior to the experiments.

METHOD DETAILS

Cell lines, culture conditions, and transfections

For protein turnover assays, cells were treated with 10 μM epoxomicin and 50 μg/mL cycloheximide (final concentration).

In vitro cell growth assay

Cell growth studies were carried out by plating 1.7 × 10^4 cells in a 24-well plate (Corning) containing 1 mL of glucose medium in triplicates. After 24hrs (Day 0), the medium was removed and replaced with fresh glucose medium or galactose medium. The galactose medium consisted of DMEM deprived of glucose (no. 11966-025; Life Technologies, Inc.), supplemented with 10 mm galactose, 2 mm glutamine (4 mm final), 10 mm HEPES, 1 mm sodium pyruvate, and 10% FCS. HeLa cells were kept in CO_2 10% at 37°C or galactose medium. At daily intervals, cells were harvested by trypsinization and counted using a hemocytometer. For rescue experiments, FBXL6 KO cells (clone 2) were seeded at 4 × 10^4. Cells were transfected with FBXL6 or GFP and counted after 48h incubation with galactose media.

Generation of control, FBXL4-, and FBXL6-KO cells

FBLX4 and FBXL6 KO HeLa cells were generated in our CRISPR facility (CRISP'EDIT University of Bordeaux, France). FBXL4 KO and FBXL6 KO HeLa cells were generated by CRISPR in wild-type HeLa cells (ATCC, ECACC 93021013). SpCas9 target sequence crRNA1-FBXL4 = Hs.Cas9.FBXL4.1.AA: CCCCACAAATCTTATACGAC and crRNA2-FBXL4 = Hs.Cas9.FBXL4.1.AB: TGGGAAGC ATTCACCTTCGT located in the exon 5 for FBXL4 and crRNA1-FBXL6 = Hs.Cas9.FBXL6.1.AA TCAGCCACAACTTGCGCATT and crRNA2-FBXL6 = Hs.Cas9.FBXL6.1.AB located in the exon 5 were designed using a CRISPOR algorithm. Single clones were then selected and PCR amplification with subsequent Sanger sequencing of the targeted FBXL4 or FBXL6 sequence were performed according the supplier's recommendations with external specific primers for FBXL4 (5′- GTGACATATTGGGCATGGGTCTAT-3′ and 5′- CCGAGGACAGCACTGCTAAAC-3′) and for FBXL6 (5′-TAGCCTGGACCTACAGCACT-3′ and 5′-CTGAAGGGGAATGCTA-3′).

Generation of GFP, FBXL4, and FBXL6 turboID cells

V5 tagged TurboID was fused to c-terminal of FBXL4 or FBXL6. Stable cell lines expressing TurboID-fusion proteins were generated by transducing HCT116 (CCL-247, ATCC) cells with lentiviral supernatant produced following the transfection (Lipofectamine 2000, Invitrogen) of 293T cells with packaging plasmids (pVSV and psPAX5) together with the pNG114 (GFP-TurboID), pNG115 (TurboID-FBXL4) or pNG116 (TurboID-FBXL6) vectors. The cells are grown at 37°C, 5% CO_2 and maintained in DMEM (Sigma) with 10% Fetal bovine serum (Gibco) and 1% Pen/strep (Gibco). Transduced cells were selected with 2μg/mL of puromycin (Invitrogene) for at least one week.

Analysis of gene expression by quantitative PCR

Total RNAs were extracted from cells using the RNeasy Plus Mini kit (Qiagen) following the manufacturer's recommendations. First strand cDNA was synthesized in a 20 μL volume using 1 μg of total RNA and iScript Reverse Transcription Supermix (Bio-Rad). PCR reactions were carried out in 25 μL volumes using SYBR Green PCR master mix (Bio-Rad) and 0.2 μM specific primers The following primer sets were deployed for real-time PCR analysis: h-FBXL4-F (TCGGGGAAGGGCCAAATAAT) and h-FBXL4-R (TTGCCCAGTATGGTTGCAGA), h-FBXL6-F (GCCAGGGGTTCAGTGAGAAG) and h-FBXL6-R (CAGGTTGAGGTAGAGCAGGC), h-RPLP0-F (GGCGACCTGGAAGTCCAACT) and h-RPLP0-R (CCATCAGCACCACAGCCTTC), h-GUSB-F (GGAGAGCTCATTTGG AATTTTGCCG) and h-GUSB-R (TGGCTACTGAGTGGGGATACCTGG), m-FBXL4-F (CCAGCTCCCAAACTTGCAGA) and m-FBXL4-R (TCAAGGATGCTGGACTTACCA), m-FBXL6-F (CCTGAGGGGTACCCGAGTTA) and m-FBXL6-R (GACACCACTGG

ACTTCCTCC), m-RPLP0-F (GGCGACCTGGAAGTCCAACT) and m-RPLP0-R (CCATCAGCACCACGGCCTTC), m-GUSB-F (TCAT CTGGAATTTCGCCG) and m-GUSB-R (CTCGGCCCTGAACCGTGACCTC). Relative quantification was done by calculating the 2ΔΔCt value.

Plasmid construction

Plasmids used in this study are listed in the key resources table. DNA cloning was performed either by DNA ligation using T4 DNA ligase (NEB), by recombination using In-Fusion HD cloning kit (Takara) or by site-directed mutagenesis using QuikChange II XL Site-Directed Mutagenesis Kit (Agilent Technologies).

FLAG tag was fused in frame of the FBXL6 full length in order to have an expression of the tag at the C-terminal of the protein. C497R mutated FBXL6-Flag was obtained using site-directed mutagenesis. MlsFBXL4-GFP and mlsFBXL6-GFP plasmids were created by PCR amplification of each mitochondrial leading sequence (mLs) predicted by MITOPROT software https://ihg.gsf.de/ihg/mitoprot.html and sub-cloning into the AscI and XhoI sites of pCMV6-AC-GFP vector (Origene). Human FBXL6 was amplified by PCR and cloned into pCMV6-Entry from Origene (CAT#: PS100001). Cyto-GFP plasmid was obtained by subcloning of eGFP into BamHI and XhoI sites of pcDNA3 vector. Cyto-GFP-CAT plasmid was created by fusion PCR of eGFP and a C-terminal Ala-Thr tail (CAT tail): briefly a DNA fragment encoding eGFP fused at the C terminus with 10 Ala-Thr repeats followed by a stop codon, was amplified by PCR using primers eGFP-infusion-BamHI-F 5′-TACCGAGCTCGGATCCGATG-3′ and eGFP-Fusion_CAT-tail-R 5' -GCTGTCGCTGTAGCGGTTGCTGTAGCCGTTGCAGTGGCCTTGTACAGCTCGTCCATG-3′ and primers eGFP-Fusion_CAT-tail-F 5′- GCAACCGCTACAGCGACAGCAACTGCCACTGCTACAGCGACTTAAATCTCGAGTCTAGAGGG-3′ and eGFP-infusion-XhoI-R 5′- GCCCTCTAGACTCGAGATTTAA-3′ and cloned into BamHI and XhoI sites of pcDNA3. Mito-GFP and mito-GFP-CAT plasmids were created by PCR amplification of the mls of COX VIIIa and subcloning into cyto-GFP and cyto-GFP-CAT plasmid respectively. A DNA fragment encoding human MRPL45 was amplified from fibroblast cDNA by RT-PCR using primers MRPL45-BamHI-F 5′-CTTGGTACCGAGCTCGGATCCATGGCAGCCCCCATACCTCAAGG-3′ and MRPL45-XbaI-HA-R 5′-GGTTTAAACGGGCCCTC TAGATTAAGCGTAATCTGGAACATCGTATGGGTACTCGAGGGCTAGCTGAGGCTTCTGGG-3′ and cloned into BamHI and XbaI sites of pcDNA3 vector. MRPL45-CAT HA plasmid was obtained by PCR amplification of CAT tail and subcloning between MRPL45 DNA and HA-tag DNA into XhoI site of MRPL45-HA plasmid. MRPL45-HA-NS plasmid was obtained by site-directed mutagenesis of three stop codons after HA-tag using two sets of primers: primers NS-1-F 5′-tgttccagattacgctttatctagagggcccgtt-3′ and NS-1-R 5′-aacgggccctctagataaagcgtaatctggaaca-3′ and primers NS-2-F 5′-agagggcccgttttaacccgcttatcagcctcgac-3′ and NS-2-R 5′-gtcgaggctgataagcgggttaaaacgggccctct-3′. All plasmids were verified by sequencing before use.

Cell fractionation and trypsin accessibility assay

The different steps of cell fractionation were performed at 4°C. Cells were harvested in mitochondrial-isolation buffer [10 mM Tris HCl (pH 7.4), 210 mM mannitol, 70 mM sucrose, and 1 mM EDTA] supplemented with protease inhibitor (Sigma-Aldrich) and homogenized by passing through a 26-gauge syringe (20 strokes). The samples were centrifuged at 500g for 5 min at 4°C. Pellet were discarded. Supernatants were collected and centrifugated at 10,000g for 15 min at 4°C. The resulting supernatant was collected as the post mitochondrial supernatant fraction (PMS). The pellets were resuspended in 1 mL of isolation buffer and submitted to another round of centrifugation. The final pellet collected and solubilized in isolation buffer. An aliquote was saved as the mitochondria-enriched fraction/crude mitochondria (CM) and the remaining CM was treated with digitonin (0.5% final) for 15 min to remove all associated membranes. This fraction was centrifugated at 10,000g for 15 min at 4°C. Pellet was collected as the purified mitochondria (PM).

Trypsin accessibility assays were performed using enriched mitochondrial fractions. These fractions were exempt of protease inhibitors. Fractions were incubated with trypsin (0.01% final) for 0, 1, 5, 15 min and 15min with 0.5% of digitonin in presence of and reactions were stop with protease inhibitors cocktails and immediately centrifuged at 10000g for 10min. We collected the pellets that we resuspended in RIPA and sample buffer.

Immunoblots

Total-cell protein lysates and subcellular fractions were prepared using 2X sample buffer supplemented with protease inhibitors. Samples were analyzed by Western blot using conventional methods. Briefly, 10 μg–40 μg proteins were separated on 4–20% acrylamide gels by electrophoresis (120 V for 1 h). Proteins were transferred to PVDF membranes using TransBlot Turbo (BioRad) 10 min at 2V. Membranes were blocked with 5% milk in phosphate-buffered saline (PBS)-Tween (0.05%) for 30 to 60 min. Proteins were detected using specific antibodies diluted in 5% milk/PBS-Tween (0.05%) and incubate from 1h to overnight according to the primary antibody used. As secondary antibodies we used horseradish peroxidase (HRP)-conjugated anti-rabbit or anti-mouse antibody (BioRad). HRP signals were visualized using chemiluminescent substrates (Thermo Fisher Scientific, Waltham, MA, USA) and acquired using a Chemidoc MP imaging system (BioRad). We also used IRDye 800CW Donkey anti-Rabbit or IRDye 680RD donkey anti-mouse IgG and revelation were performed using odyssey imaging system (Licor).

Images analyses were quantified using ImageJ (NIH) for chemiluminescent signal or using Image Studio lite 5.2 (licor) for fluorescence signals.

BN-PAGE

Aggregation of endogenous MRPL45 was investigated in whole FBXL4-KO, FBXL6-KO, and control cell extracts using BN-PAGE. Samples were prepared at 4°C. Cells grown in 10 cm dishes were scrapped on ice and washed with cold PBS. Cell pellets were solubilized for 30 min on ice in 1X NativePAGE Sample Buffer (Invitrogen) containing protease inhibitors and 1.0% digitonin and then, centrifuged at 16,000x*g* for 20 min at 4°C. Supernatants were collected and the protein concentration was determined using the BCA method. Prior to electrophoresis, the samples were supplemented with 0.25% Coomassie blue G (final concentration). For the first native dimension, 40 μg of protein was separated on 4–16% gradient native-PAGE gels (NativePAGE Novex Bis-Tris Gel from Invitrogen). Electrophoresis was performed using a light cathode buffer (NativePAGE 1X Running Buffer plus 0.02% G-250) and an anode buffer (NativePAGE 1X Running Buffer). Electrophoresis was performed at 150 v for about 2 h at room temperature.

Then, the gel strips were excised from the gels and incubated with 2X sample buffer containing 50 mM dithiothreitol (DTT) for 20 min. The lanes were placed on IPG tris/SDS gels (Biorad) and electrophoresis under denaturating conditions was performed using an SDS running buffer. Next, immunoblotting was performed following classical procedures.

Immunoprecipitation

For co-immunoprecipitation assays, HEK cells were transfected 48h before the assays. Cells transfected with β-galactosidase were used as control. Cells were scrapped and washed with cold PBS. Cell pellets were solubilized using IP lysis buffer (1% Triton X-100, 50 mM Tris (pH 7.4), 150 mM NaCl, 10 mM EDTA) supplemented with protease inhibitors. Solubilizations were performed for 20 min at 4°C with rotating mixing. Then, debris were removed by centrifugation for 20 min at 16,000g. Supernatants were incubated for 4h with anti-Flag or Ha agarose beads (Thermo Fisher Scientific and Merck) at 4°C with rotating mixing. Agarose beads were collected by centrifugation (30 s at 3000rpm). Beads were washed five times with cold PBS 0.05% Tween. Elution of proteins were performed using 2X Laemmli sample buffer (Merck) at 90°C for 5 min. Samples were analyzed by mass spectrometry as described above or immunoblots. For mass spectrometry, interactions were considered significant when each biological replicate displayed at least 2-fold enrichment as compared to control.

Proteome analyses by mass spectrometry

Ten μg of proteins were loaded on a 10% acrylamide SDS-PAGE gel and proteins were visualized by Colloidal Blue staining. Migration was stopped when samples had just entered the resolving gel and the unresolved region of the gel was cut into only one segment. Each SDS-PAGE band was cut into 1 mm × 1 mm gel pieces. Gel pieces were destained in 25 mM ammonium bicarbonate (NH4HCO3), 50% Acetonitrile (ACN) and shrunk in ACN for 10 min. After ACN removal, gel pieces were dried at room temperature. Proteins were first reduced in 10 mM dithiothreitol, 100 mM NH4HCO3 for 60 min at 56°C then alkylated in 100 mM iodoacetamide, 100 mM NH4HCO3 for 60 min at room temperature and shrunken in ACN for 10 min. After ACN removal, gel pieces were rehydrated with 50 mM NH4HCO3 for 10 min at room temperature. Before protein digestion, gel pieces were shrunken in ACN for 10 min and dried at room temperature. Proteins were digested by incubating each gel slice with 10 ng/μL of trypsin (V5111, Promega) in 40 mM NH4HCO3, rehydrated at 4°C for 10 min, and finally incubated overnight at 37°C. The resulting peptides were extracted from the gel by three steps: a first incubation in 40 mM NH4HCO3 for 15 min at room temperature and two incubations in 47.5% ACN, 5% formic acid for 15 min at room temperature. The three collected extractions were pooled with the initial digestion supernatant, dried in a SpeedVac, and resuspended with 0.1% formic acid for a final concentration of 0.05 μg/μL. NanoLC-MS/MS analysis were performed using an Ultimate 3000 RSLC Nano-UPHLC system (Thermo Scientific, USA) coupled to a nanospray Orbitrap Fusion Lumos Tribrid Mass Spectrometer (Thermo Fisher Scientific, California, USA). Each peptide extracts were loaded on a 300 μm ID x 5 mm PepMap C18 precolumn (Thermo Scientific, USA) at a flow rate of 10 μL/min. After a 3 min desalting step, peptides were separated on a 50 cm EasySpray column (75 μm ID, 2 μm C18 beads, 100 Å pore size, ES803A rev.2, Thermo Fisher Scientific) with a 4–40% linear gradient of solvent B (0.1% formic acid in 80% ACN) in 57 min. The separation flow rate was set at 300 nL/min. The mass spectrometer operated in positive ion mode at a 2.0 kV needle voltage. Data was acquired using Xcalibur 4.1 software in a data-dependent mode. MS scans (m/z 375–1500) were recorded at a resolution of R = 120000 (@ m/z 200) and an AGC target of 4 × 105 ions collected within 50 ms, followed by a top speed duty cycle of up to 3 s for MS/MS acquisition. Precursor ions (2–7 charge states) were isolated in the quadrupole with a mass window of 1.6 Th and fragmented with HCD@30% normalized collision energy. MS/MS data was acquired in the ion trap with rapid scan mode, AGC target of 3 × 103 ions and a maximum injection time of 35 ms. Selected precursors were excluded for 60 s. Protein identification and Label-Free Quantification (LFQ) were done in Proteome Discoverer 2.4. MS Amanda 2.0, Sequest HT and Mascot 2.5 algorithms were used for protein identification in batch mode by searching against a Uniprot Homo sapiens database (75 093 entries, release May 10, 2020). Two missed enzyme cleavages were allowed for the trypsin. Mass tolerances in MS and MS/MS were set to 10 ppm and 0.6 Da. Oxidation (M), acetylation (K) and deamidation (N, Q) were searched as dynamic modifications and carbamidomethylation, (C) as static modification.

Raw LC-MS/MS data were imported in Proline Web[43] for feature detection, alignment, and quantification. Proteins identification was accepted only with at least 2 specific peptides with a pretty rank = 1 and with a protein FDR value less than 1.0% calculated using the ''decoy'' option in Mascot. Label-free quantification of MS1 level by extracted ion chromatograms (XIC) was carried out with parameters indicated previously.[44] For expression analysis, the normalization was carried out on median of ratios. An inference of missing values was applied with 5% of the background noise when analyzing whole FBXL6-KO and control cell proteome. For

immunoprecipitation data, no normalization or inference was applied. A Wilcoxon-Mann-Whitney test was applied to test the significance of the variation in relative protein abundances between experimental conditions.

Pulsed SILAC assay

SILAC media was prepared as described by Ong and Mann.[45] Light media contains DMEM supplemented with 10% dialyzed FBS, Pen/Strep 1X; L-lysine (146mg.L^{-1}) f, L-arginine (84mg.L^{-1}) and proline (20mg.L^{-1}). In heavy media, L-lysine and L-Arginine were replaced by L-lysine ^{13}C6 (180mg.L^{-1}) and ^{13}C6 L-arginine (88mg.L^{-1}), respectively. HEK cells were grown in light media for 2 weeks before uses. Two days before changing the media, cells were transfected with FBXL6-flag or control plasmid expressing β-galactosidase. At t = 0h, cells were shifted to heavy media for 3h. Then, we performed a flag IP as described above and we saved an input fraction. Both input and pulled down fraction were subject to mass spectrometry analyses (see above). For pulsed SILAC, ^{13}C-K and ^{13}C-R were searched as static modifications.

Turbo ID and mass spectrometry analysis

TurboID proximity labeling is based on previously described protocol (Cho et al., 2020). Briefly, TurboID was fused to the C terminus of GFP or FBXL6. HCT116 stable cell line expressing FBXL6-TurboID and TurboID-GFP were grown for 30 min and 16 h in presence of 50 μM of biotin (Sigma Aldrich). About 20 million cells (two 10-cm plates) were first washed two times with ice-cold PBS and lysed in 1 mL of RIPA buffer (50 mM Tris HCL, pH 7.4; 150 mM NaCl, 0.1% SDS, 0.5% Sodium Deoxycholate, 1% Triton 100X) for 10 min on ice. The extract is sonicated 3 times at 20% amplitude for 20 s and cleared by centrifugation at 12 000 g for 10 min. The supernatant kept to pulldown biotinylated proteins by the addition of 100 μL of streptavidin-coupled magnetic beads slurry (Streptavidin Mag Sepharose, GE Healthcare) previously washed and equilibrated. Samples are put on rotating wheel overnight at 4°C. The beads are washed 5 min at RT on rotating wheel, twice with RIPA buffer, once with 1M KCL, with 0.1M Na2CO3 and with 2M urea in 10mM Tris-HCL pH8. Beads are washed again twice with RIPA buffer and with 50 mM NH4HCO3. A fraction of the beads (5%) is boiled in Laemmli buffer for western blotting and the remaining beads are analyzed by LC/MS-MS.

For mass spectrometry analyses, magnetic beads were extensively washed in 50 mM ammonium bicarbonate and proteins were digested directly on the beads in 2 consecutive steps with sequencing-grade porcine trypsin (Promega, Fitchburg, MA, USA). Peptides generated after trypsin digestion were analyzed by nanoLC-MS/MS on a QExactive + mass spectrometer coupled to an EASY-nanoLC-1000 (Thermo-Fisher Scientific, USA). Peptides were identified with Mascot algorithm (Matrix Science, London, UK): the data were searched against the Swissprot updated databases with Homo sapiens taxonomies using the software's decoy strategy. Mascot 2.6 and Swissprot version 2020_05 (20386 sequences) were used for the experiment. Mascot identifications were imported into Proline 1.4 software (Bouyssié et al. 2020) where they were validated using the following settings: PSM score ≤25, Mascot pretty rank < = 1, FDR < = 1% for PSM scores, FDR < = 1% and for protein set scores. The total number of MS/MS fragmentation spectra was used to quantify each protein.

For the statistical analysis of the data, we compared the different samples against the negative controls using R v3.5.2 and R-studio. The spectral counts from 3 replicates were normalized according to the DESeq2 normalization method (i.e., median of ratios method) and EdgeR was used to perform a negative-binomial test. For each identified protein, an adjusted p value (adjp) corrected by Benjamini–Hochberg was calculated, as well as a protein fold-change (FC). The results are presented in a Volcano plot using protein log2 fold changes and their corresponding adjusted (-log10adjp) to highlight up regulated and down regulated proteins.

Immunofluorescence microscopy

Cells were grown on glass coverslips and transfected using Fugene HD (Promega). After 24 h-48h, cells were fixed with 4% paraformaldehyde for 15 min at room temperature (all of the following steps were done at room temperature) and then, PFA was washed out with phosphate-buffered saline. Cells were permeabilized in 0.2% Triton X-100–phosphate-buffered saline for 15 min and saturated with 10% bovine serum albumin in PBS for 45 min. Primary antibodies were incubated for 2 h in the blocking buffer (10% BSA in PBS). Three washes of 10 min with blocking buffer were performed before incubation with secondary antibodies for 45 min. Following three washes of 10 min with PBS, immunostainings were visualized with a Zeiss microscope. Images were acquired using a Zeiss microscope (AxioZision; Carl Zeiss, OberKOchen, Germany) with a 63× objective. Z sections (interval: 0.2 μm) covering the entire depth of the cell were acquired. Quantifications (levels of fluorescence and Pearson's correlation coefficient) were performed using Zeiss co-localization software (Carl Zeiss).

Oxygen consumption analyses and ATP measurement

To measured cellular oxygen consumption rate, cells were grown on 10cm dishes and 24h before testing, growing media were replaced by no glucose media supplemented with glutamine. Cells were collected and resuspended to 1 × 10^6 cells/mL in glutamine media.

Cellular respiration was measured from 1 × 10^6 cells/mL to 5 × 10^6 cells/mL at 37°C. Mitochondrial oxygen-consumption assays were performed using the high-resolution respirometry system Oxygraph-2k (Oroboros). The basal respiration, the oligomycin- and the FCCP-dependent respiration were successively recorded over the time.

To assay ATP content, cells were seeded in a 96-well white plate with a clear bottom at 8000 cells per well. The following day, the intracellular ATP content was measured by using the bioluminescent ATP Kit CellTiter-Glo 2.0 (Promega) following the

manufacturer's instructions. The part of ATP produced by mitochondria was calculated as the difference between the total ATP content and the amount of ATP measured in the presence of the ATP synthase inhibitor oligomycin. Cells were incubated 30 min with 3 μM oligomycin to inhibit mitochondrial respiration and linked-ATP synthesis before adding the CellTiter-Glo 2.0 Reagent to the wells. Luminescence was measured by a multiplate reader (Luminoskan Microplate Luminometer, Thermo Fisher Scientific, Waltham, MA, USA). Standardization was performed with known quantities of standard ATP in the same conditions.

Cell cycle assays

Cell was incubated for 48h in glucose or glutamine medium. Edu labelling was carried out according manufacturer recommendation (Thermofisher Click it Edu). Briefly, Edu 10μM was added for 1.5 h. Fixed and permeabilized cells were incubated with RNase for 2 h 37°C before Alexa 647 Click it Edu Reaction. Then, cells were incubated 20 min for DNA content with a 10% dilution IP/Rnase (FxCycle, Invitrogen) and analyzed by Facs (BD Accuri C6 plus).

Graphical methods

Cartoon scheme and graphical abstract were generated using Biorender.

QUANTIFICATION AND STATISTICAL ANALYSIS

All values represent the mean ± SEM. Statistical analyses were performed using the Prism 9 software (GraphPad). Normality distribution was assessed using the D'Agostino-Pearson test. The p value, tests, and post hoc tests are cited in the figure legend.

Gene Ontology analyses were performed using DAVID 6.8.[46] We selected GOTERM_BP_DIRECT pathways containing at least three proteins. For HeLa cells we used background from Robin et al.[47] and for HEK cells Lavado-Garcia et al.[48] We used proteins presenting significantly ($p < 0.05$) increased or decreased expression following mass spectrometry analyses.